AFRL-RV-PS-
TR-2018-0150

AFRL-RV-PS-
TR-2018-0150

HIGH ENERGY ALL-SOLID-STATE LI-ION BATTERIES

Sehee Lee

Regents of the University of Colorado
3100 Marine St., Rm 479
Boulder, CO 80303-1058

03 February 2019

Final Report

AIR FORCE RESEARCH LABORATORY
Space Vehicles Directorate
3550 Aberdeen Ave SE
AIR FORCE MATERIEL COMMAND
KIRTLAND AIR FORCE BASE, NM 87117-5776

DTIC COPY

NOTICE AND SIGNATURE PAGE

Using Government drawings, specifications, or other data included in this document for any purpose other than Government procurement does not in any way obligate the U.S. Government. The fact that the Government formulated or supplied the drawings, specifications, or other data does not license the holder or any other person or corporation; or convey any rights or permission to manufacture, use, or sell any patented invention that may relate to them.

This report is the result of contracted fundamental research which is exempt from public affairs security and policy review in accordance with AFI 61-201, paragraph 2.3.5.1. This report is available to the general public, including foreign nationals. Copies may be obtained from the Defense Technical Information Center (DTIC) (http://www.dtic.mil).

AFRL-RV-PS-TR-2018-0150 HAS BEEN REVIEWED AND IS APPROVED FOR PUBLICATION IN ACCORDANCE WITH ASSIGNED DISTRIBUTION STATEMENT.

//signed//

JESSICA BUCKNER
Program Manager

//signed//

DAVID WILT
Tech Advisor, Spacecraft Component Technology Branch

//signed//

JOHN BEAUCHEMIN
Chief Engineer, Spacecraft Technology Division
Space Vehicles Directorate

This report is published in the interest of scientific and technical information exchange, and its publication does not constitute the Government's approval or disapproval of its ideas or findings.

REPORT DOCUMENTATION PAGE

Form Approved
OMB No. 0704-0188

1. REPORT DATE *(DD-MM-YYYY)*	**2. REPORT TYPE**	**3. DATES COVERED *(From - To)***
03-02-2019	Final Report	03 Feb 2015 – 03 Feb 2019

4. TITLE AND SUBTITLE

High Energy All-Solid-State Li-ion Batteries

5a. CONTRACT NUMBER
FA9453-15-1-0304

5b. GRANT NUMBER

5c. PROGRAM ELEMENT NUMBER
62601F

6. AUTHOR(S)

Sehee Lee

5d. PROJECT NUMBER
8809

5e. TASK NUMBER
PPM00020597

5f. WORK UNIT NUMBER
EF126032

7. PERFORMING ORGANIZATION NAME(S) AND ADDRESS(ES)

Regents of the University of Colorado
3100 Marine St., Rm 479
Boulder, CO 80303-1058

8. PERFORMING ORGANIZATION REPORT NUMBER

9. SPONSORING / MONITORING AGENCY NAME(S) AND ADDRESS(ES)

Air Force Research Laboratory
Space Vehicles Directorate
3550 Aberdeen Ave., SE
Kirtland AFB, NM 87117-5776

10. SPONSOR/MONITOR'S ACRONYM(S)
AFRL/RVSV

11. SPONSOR/MONITOR'S REPORT NUMBER(S)
AFRL-RV-PS-TR-2018-0150

12. DISTRIBUTION / AVAILABILITY STATEMENT
Approved for public release; distribution is unlimited.

13. SUPPLEMENTARY NOTES

14. ABSTRACT

Over the course of this project, we have developed high capacity all-solid-state Li-ion battery anodes using a variety of different approaches and manufacturing processes. The most promising of these techniques has been the utilization of commercially available polyacrylonitrile as a mixed conducting binder. Through the use of this inexpensive and tough polymer, we have demonstrated stable cycling, high capacity electrodes with large mass loadings of silicon and tin active materials. The optimization of the silicon-polyacrylonitrile sheet style anode has resulted in a cell displaying a large electrode specific capacity >1300 mAh/g with over 91% capacity retention after 100 charge-discharge cycles. This is, to our knowledge, the best cycling performance ever reported for an all-solid-state Li-ion anode.

15. SUBJECT TERMS
lithium rich cathode, carbon nanotubes, solid state battery, specific energy>= 350 Wh/kg, Li-ion cathodes, space power

16. SECURITY CLASSIFICATION OF:			**17. LIMITATION OF ABSTRACT**	**18. NUMBER OF PAGES**	**19a. NAME OF RESPONSIBLE PERSON**
a. REPORT	**b. ABSTRACT**	**c. THIS PAGE**			Jessica Buckner
Unclassified	Unclassified	Unclassified	SAR	62	**19b. TELEPHONE NUMBER *(include area code)***

Standard Form 298 (Rev. 8-98)
Prescribed by ANSI Std. 239.18

(This page intentionally left blank)

TABLE OF CONTENTS

Section **Page**

LIST OF FIGURES

Figure **Page**

ACKNOWLEDGMENTS

This material is based on research sponsored by Air Force Research Laboratory under agreement number FA9453-15-1-0304. The U.S. Government is authorized to reproduce and distribute reprints for Governmental purposes notwithstanding any copyright notation thereon. The views and conclusions contained herein are those of the authors and should not be interpreted as necessarily representing the official policies or endorsements, either expressed or implied, of Air Force Research Laboratory or the U.S. Government

1 SUMMARY

Over the course of this project, we have developed high capacity all-solid-state Li-ion battery anodes using a variety of different approaches and manufacturing processes. The most promising of these techniques has been the utilization of commercially available polyacrylonitrile as a mixed conducting binder. Through the use of this inexpensive, tough polymer, we have demonstrated stable cycling, high capacity electrodes with large mass loadings of silicon and tin active materials. This is, to our knowledge, the first time these high capacity lithium-alloying materials have been utilized in a slurry-coated all-solid-state Li-ion battery anode. The early optimization of the silicon-polyacrylonitrile sheet style anode has resulted in a cell displaying a large electrode specific capacity >1300 mAh/g with over 91% capacity retention after 100 charge-discharge cycles. This is, to our knowledge, the best cycling performance ever reported for an all-solid-state Li-ion anode; it even ranks as one of the top practical anodes ever published for any Li-ion cell configuration. We believe that our work represents a step forward for slurry-coated electrodes and that the continued development of these high capacity sheet-style anodes will be critical to the commercialization of the all-solid-state Li-ion battery.

2 INTRODUCTION

Bulk all-solid-state batteries are a safe alternative to conventional Li-ion batteries because their mechanochemically prepared sulfide based electrolytes [1-3] are non-volatile, non-flammable, and stable versus lithium metal. However, the use of a lithium metal anode in an all-solid-state battery (ASSB) is not straightforward as lithium dendrites can still probe through the dense ceramic electrolyte separator layers [4]. This penetration of lithium through the cell results in short circuiting, limiting the use of lithium metal anodes to relatively modest cycling parameters. Therefore, in order to realize the secondary ASSB, high capacity, practical alternatives to the lithium metal anode must be developed.

Many alternative anodes have been presented in the literature, but few have been able to meet the requirements of low cost, high capacity and scalability while maintaining acceptable cycling performance. For example, some researchers have utilized InLi [5,6] or $Li_{4.4}Ge_xSi_{1-x}$ [7] alloys to avoid the short-circuiting associated with lithium metal anodes, but the high cost of indium and germanium make these solutions impractical for commercial applications. Graphite [8,9], which has seen widespread use in conventional lithium ion batteries (LIBs), is inexpensive and readily available, but its low theoretical capacity (372 mAh/g) greatly limits the achievable energy density of a cell. Many state of the art materials boasting large, stable capacities rely on complex nanostructured materials, such as Si nanowires [10], core-shell Si nanowires [11] and hollow Si nanostructures [12]. While the performance of these active materials is impressive, they require complex manufacturing processes impractical for mass production.

Two promising anode materials for the next generation of Li-ion batteries are silicon and tin. Silicon is attractive due to its low operating potential (< 0.5 V vs Li^+/Li), earth abundance and large room temperature theoretical specific capacity, 3579 mAh/g ($Li_{15}Si_4$). Tin, on the other hand, displays outstanding electrical conductivity ($9.17x10^6$ S/m) and Li-ion diffusivity ($5.9x10^{-7}$ cm^2/s of $Li_{4.4}Sn$) with relatively large gravimetric and volumetric capacities (959 mAh/g and 2,476 mAh/mL for 4.25 Li-ions) [13, 14]. Unfortunately, both silicon and tin experience large

volumetric expansions (>200%) upon lithiation, which usually results in electrode pulverization, active material isolation and irreversible capacity loss with cycling.

Over the course of this project, we developed a variety of high capacity all-solid-state Li-ion battery electrodes. We first investigated the use of a Si-Ti-Ni (STN) ternary alloy for use in commercial all-solid-state Li-ion cells [15]. The STN alloy has a microstructure of nano-Si particle domains embedded in an electrochemically active $Ti_4Ni_4Si_7$ matrix. During the initial lithiation of the STN alloy, the matrix irreversibly takes up some Li^+ to become a mixed conductor with an approximate composition of $Li_{3.2}Ti_4Ni_4Si_7$ and an ionic conductivity of 2.0 x 10^{-5} S cm^{-1}. We applied the STN alloy to an all-solid-state battery because the $Li_xTi_4Ni_4Si_7$ matrix provides fast ionic conduction to the embedded nano-Si particles. We reported that an all-solid-state STN anode achieved a stable specific capacity of 405 mAh g^{-1} (electrode).

To realize a full cell, we paired our STN composite anode with our previously described iron sulfide and sulfur (FeS + S) cathode [16]. The pairing of a lithium free FeS + S cathode and a lithium free STN anode presented an easily overcome obstacle. Our Li_3N decomposition pre-lithiation technique was not appropriate for conversion materials or for anodes with operating voltages less than 0.44 V vs. Li^+/Li [17] so we adopted a lithiation technique utilizing stabilized lithium metal powder (SLMP). Previously, this method had only been demonstrated in conventional liquid cells [18,19].

Next, we investigated coal-tar-pitch (CTP) as an inexpensive precursor to prepare an amorphous carbon matrix material. This black, sooty material is composed of cyclical hydrocarbons with widely ranging molecular weights and configurations [20]. We showed that the pyrolysis of CTP produces a mixed conducting amorphous carbon with impressive electrochemical properties. Through a simple and industrially scalable solution coating process, we were able to inexpensively produce Si-C composite particles capable of being cycled in an all-solid-state cell. While the use of similar Si-C composites had been reported in conventional coin-cells, we are, to our knowledge, the first to demonstrate this anode material's potential in an all-solid-state cell [21]. In fact, the use of this electrochemically active Si-C composite enabled an all-solid-state half cell to maintain a stable anode specific capacity >650 mAh/g after 100 charge-discharge cycles.

To prevent irreversible capacity loss, it is important to maintain a high degree of electrochemical connectivity between the active materials in a LIB electrode. This is especially important in an ASSB where the electrolyte is not capable of penetrating the electrode to provide Li-ion transport in situ. Commonly, large amounts of inactive conductive additives (solid electrolytes and carbon) are mixed in with the active materials to link them with both Li-ion and electron transport channels throughout the electrode. These conductive additives reduce the volumetric and gravimetric capacities of the electrode and limit the practical mass loading of active materials. Furthermore, mixing and pressing conductive additive powders does not commonly result in a high degree of interfacial coupling with rigid active materials such as silicon. Instead, this processing technique restricts conduction pathways to bottlenecks at small particle-particle contact points. Figure 1a shows how the unrestricted expansion and eventual cracking of active materials like silicon and tin can easily disrupt these small points of contact in a conventional pressed powder composite all-solid-state electrode. This leaves the active materials electrochemically isolated and their capacity irreversibly lost to the cell.

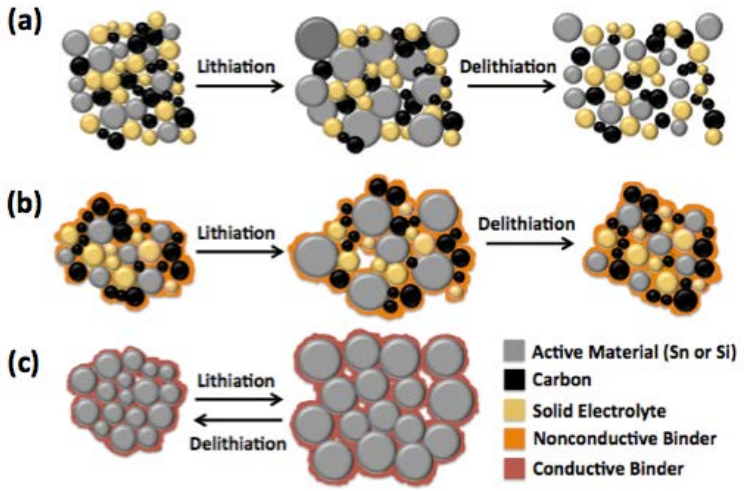

Figure 1. Schematics of All-Solid-State Electrode Architectures

While our success with electrochemically active, mixed conducting matrix materials enabled us to achieve unprecedented capacities, these all-solid-state electrodes still relied on the mixing and pressing of powders to compact active materials within a dense secondary matrix of ionically conductive solid electrolyte. To progress the ASSB towards commercialization, steps must be taken to move away from this bulk pressed-pellet construction. Instead, slurry coated or "sheet" style electrodes must be developed for use in all-solid-state cells (Figure 1b). Sheet style electrodes are prepared by mixing active material and conductive additives into a binder and solvent solution. The resulting slurry can then be bladed onto a thin foil current collector. This allows for the mass production of energy dense electrodes via the roll-to-roll processes already utilized in conventional Li-ion battery manufacturing.

To date, there has been a limited amount of research published on the use of slurry coated sheet style electrodes in ASSBs [22-24]. In fact, all of the solid-state sheet style anodes reported thus far have been composite electrodes (Figure 1b) utilizing small mass loadings (<60 wt%) of graphite active materials with non-conductive polymer binders. While this architecture works well with low capacity intercalation materials (e.g. graphite), slurry coated composite electrodes had not yet been shown effective in utilizing high capacity Li-alloying materials such as tin and silicon in an all-solid-state cell. This is because the conductive additives used in these electrodes are not flexible enough to accommodate the extreme volume changes associated with the lithiation/delithiation of these materials.

We have overcome this issue by conformally encapsulating tin nanoparticles in a thin layer of mixed conducting polyacrylonitrile (PAN) binder (Figure 1c). PAN is a unique material. In its virgin state, PAN is a tough, insulating, linear polymer defined by its triple bonded nitrile groups (Figure 2a). The high polarity of these nitrile groups allows PAN to homogeneously coat and strongly adhere to the surface of both the active particles and current collector via powerful intermolecular forces [25]. PAN is also interesting in that despite being a thermoplastic, it does not melt at normal heating rates. Instead, the heat treatment of PAN degrades the polymer into an infusible, non-flammable, stabilized structure before it can melt [26]. If this stabilization process is conducted at temperatures exceeding 600°C, the PAN structure will break down into graphite like domains. This has led PAN to become a dominant precursor in the manufacturing of high strength carbon fibers [26-28]. Alternatively, if heat treatment temperatures are limited to 250-350°C, carbonization is avoided and the polymer's triple bonded nitrile groups cyclize into the

partly aromatic conjugated ladder structure depicted in Figure 2b [26,27,29,30]. This low temperature cyclization allows the PAN to retain much of its polymeric toughness while introducing intrinsic electric conductivity via delocalized sp^2 π bonding in its conjugated pyridinic rings [31]. The extent of the cyclization, or "zip-length", is expected to be no more than 2-5 consecutive nitrile groups on average [32]. This is because PAN's linear chains form irregular rod-like helical structures due to the strong intramolecular dipole repulsions of their nitrile groups [26]. So, in order for the exothermic intramolecular cyclization reaction to occur, adjacent isotactic nitriles would need to align by unwinding their chain's backbone. Since unwinding the coiled chain would result in an unfavorable decrease in its entropy, the zip-length of cyclization propagation along the chain is thought to be limited. Alternatively, a relatively large degree of intermolecular polymerization is believed to occur between the closely packed helical chains. Because the highly polar nitrile groups of adjacent PAN chains will naturally pair in low energy antiparallel arrangements, non-cyclic conjugated crosslinks are expected to readily form between neighboring chains. This gives a full picture of the thermally stabilized PAN binder as a network of chains composed of small, cyclized ladder segments connected by flexible unreacted C-C bonded segments which are all bound together by strong conjugated intermolecular crosslinks (Figure 2c).

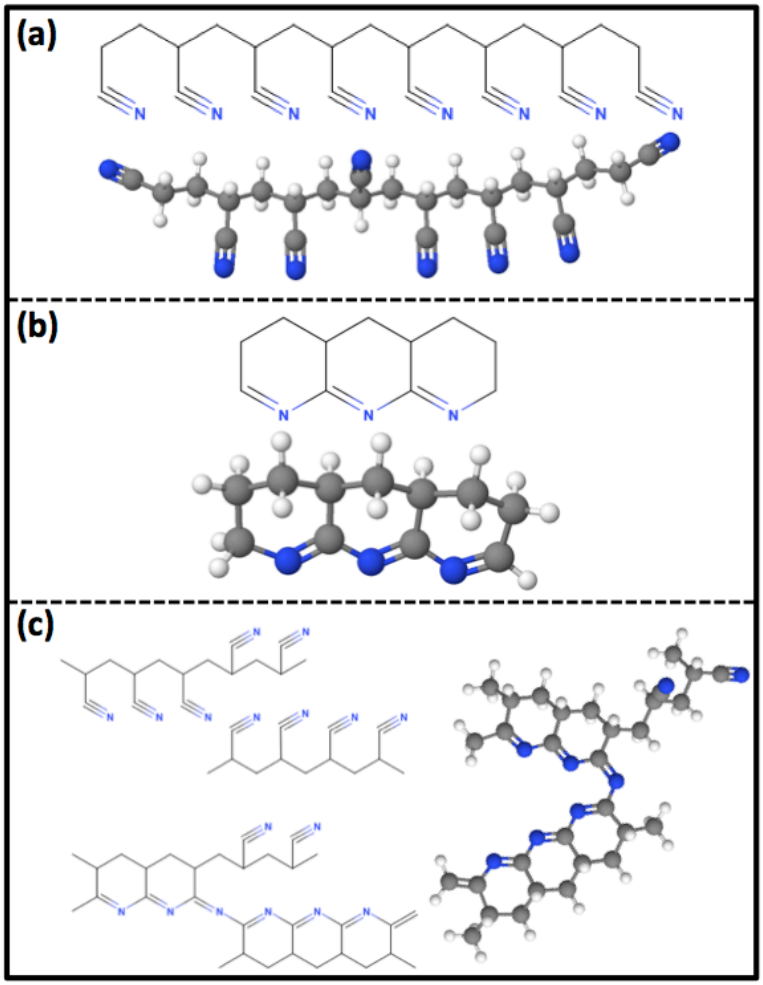

Figure 2. Atomic Structure of Polyacrylonitrile (PAN) Chains Before and After Heat Treatment

As mentioned above, the low temperature cyclization process transforms commercially available PAN into an ideal binder for high capacity all-solid-state sheet style anodes. The cyclized PAN's conjugated ladder structures introduce intrinsic electric conductivity to the electrode. This removes the need for inactive conductive carbon additives that can leave the active tin particles isolated with cycling. Furthermore, the insitu intermolecular crosslinking increases connectivity between the chains, strengthening the binder. Lastly, the presence of unreacted segments in the heat treated PAN is vitally important for three separate reasons. For one, the freely rotating C-C bonding in these segments ensures that the binder remains flexible. This allows the cyclized PAN (cPAN) binder to withstand the large volume changes associated with the lithiation/delithiation of tin particles without fracturing or delaminating. Secondly, the strong polar nature of these bonds increases the adhesion of the cPAN to both the active materials and current collector. Finally, these unreacted nitrile groups are thought be the key to the cPAN binder's ionic conductivity. On its own, pure PAN is known to be a relatively poor Li-ion conductor (~10^{-14} S/cm) [33]. While pure PAN is far too resistive to be useful as a solid polymer electrolyte, our previous reports on silicon-cPAN anodes cycled in conventional Li-ion cells points out that its conductivity is sufficient enough to enable outstanding performance at fast 5C rates [31, 34]. At that time we did not present a possible mechanism for ion conduction in the cPAN binder. We now postulate that the Li-ions diffuse through the thin cPAN layers with the help the binder's unreacted nitrile groups. Specifically, we believe that the empty 2s orbital of Li^+ forms an ion associate with the lone pair of electrons on the nitrile group's highly electronegative nitrogen atom. In fact, the presence of these $[Li{:}\,N \equiv C - R]^+$ associates has previously been confirmed by both Raman and IR spectroscopy [35-38]. We therefore suggest that the mobile Li-ions travel from unreacted nitrile group to adjacent unreacted nitrile group in the cPAN binder, aided by the segmental motion of the partially cyclized chains. This mechanism is quite similar to that of the well established poly(ethylene oxide) (PEO) and poly(propylene oxide) (PPO) electrolyte systems where Li-ions are known to associate with the polymers' electronegative oxygen atoms. And while these PEO and PPO solid polymer electrolytes are heavily modified with plasticizing solvents in order to increase their chain dynamics and boost their conductivity, the modest Li-ion conductivity of the cPAN binder has proved sufficient for use in sheet style all-solid-state anodes.

Due to the unique properties of the insitu stabilized cPAN binder, we are the first to demonstrate the utilization of high capacity lithium alloying materials in an all-solid-state sheet style anode. The strong adhesion and conformal coating of this mixed conducting polymer has allowed us to reversibly cycle a slurry coated nano tin and silicon electrodes without the need for additional inactive conductive additives such as solid electrolyte or carbon. This results in outstanding cycling performance while greatly boosting the volumetric and gravimetric capacity of the electrode.

3 METHODS, ASSUMPTIONS, AND PROCEDURES

All of the cell fabrication and testing outlined in this report was carried out in an inert argon environment. The glassy sulfide solid electrolyte (SSE) used in these cells, $77.5Li_2S{:}22.5P_2S_5$, was prepared by mechanical milling. Detailed discussion of this mechanochemical synthesis has been previously reported [39].

The FeS + S cathode was prepared by mechanochemically combining FeS and S precursors with the SSE [16]. The pre-lithiated Si-Ti-Ni (STN) alloy anode was fabricated in a two-step process. First, STN powder (MK electron, 66 at. % Si, air jet milled) [15], SSE, and carbon black (TimCal, C65) were mixed with an agate mortar and pestle in a ratio of either 7:3:0 or 7:3:2, respectively. Stabilized lithium metal powder (SLMP, FMC Lithium Corp., Lectro Max powder 100) was then combined with the 7:3:2 composition STN anode powder via vortex mixing (Vortex Genie 2) in a weight ratio of 1 to 5.21, respectively.

To measure the electronic conductivity of the STN matrix, $Ti_4Ni_4Si_7$ and $Li_{3.2}Ti_4Ni_4Si_7$ were prepared as described elsewhere [15]. A potential sweep was then applied to cold-compacted pellets of $Ti_4Ni_4Si_7$ and $Li_{3.2}Ti_4Ni_4Si_7$ using Ti current collectors. The shell of our all-solid-state batteries is a titanium- polyetheretherketone (PEEK) test cell die (Figure 3). To fabricate each cell, the amorphous SSE powder was compressed to 1 metric ton inside the Ti-PEEK die to form the separator pellet. 5 mg of the FeS + S cathode powder and 8.36 mg of the pre-lithiated STN anode powder were then cold-pressed to opposite sides of the glass electrolyte pellet with 5 metric tons force.

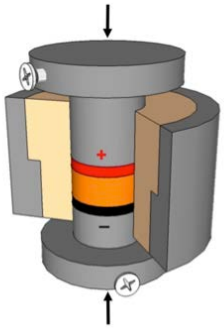

Figure 3. Schematic of our All-Solid-State Battery Test Dies

The Si-C composite anode materials presented in this report were prepared by first adding 0.5 g coal-tar-pitch (Mitsubishi Chemical) and 0.5 g silicon powders (325 mesh [≤44 μm], Aldrich, 99%; 1-3 μm, US Research Nanomaterials, 99.9% or 50 nm, Alfa Aesar, 98%) to a screw-top glass vial containing 2.5 g N,N-Dimethylformamide (DMF) solvent (Fischer). The contents of this vial were mixed overnight with a magnetic stir bar in order to fully dissolve the pitch powders and evenly disperse the silicon particles. After two hours in a sonication bath, this slurry was evenly spread over copper foil and dried in an oven at 60°C. With the DMF fully evaporated, the silicon-pitch composite could be scraped away from the copper foil and heat-treated in a tube furnace for five hours at 900°C under continuous argon gas flow. The same heat treatment procedure was applied to a sample of pure pitch powder so that its structure and electrochemical activity could be characterized. A consistent pitch mass loss of ~35% was observed after pyrolysis, signifying that the composition of the Si-C composites was roughly 60% silicon and 40% carbon matrix, by mass.

All-solid-state cells were constructed and cycled within our 13 mm diameter polyetheretherketone (PEEK) lined titanium dies, with two titanium plungers acting as current collectors. Titanium was used as the plunger / current collector material because of its mechanical strength and wide window of electrochemical stability. To construct an all-solid-state half-cell, 150 mg of amorphous solid-state electrolyte (SSE) powder was first pressed into a relatively dense, ionically conductive separator pellet. Composite working electrodes were prepared by hand mixing the Si-C active materials with SSE using a mortar and pestle. After mixing, 2 mg of this electrode composite was evenly spread on one side of the solid electrolyte pellet. On the opposing side, 100 mg of indium-lithium (InLi) alloy was added as a counter electrode. After depositing both electrodes, a hydraulic hand press was used to compress the all-solid-state half-cell with five metric tons of force. This final cold pressing densifies the all-solid-state half-cell pellet, improving interfacial contact within and between its three layers.

The InLi counter electrode material was prepared by vortex mixing (vortex genie 2) stoichiometric amounts of indium and stabilized lithium metal powder (SLMP, FMC Lithium Corp., Lectro Max Powder 100) in a glass vial. The InLi alloy, which has a potential of 0.62 V versus Li^+/Li, was prepared by vortex mixing (Vortex Genie 2) appropriate amounts of Indium (Alfa Aesar, Puratronic 99.999%) and Lithium (FMC Lithium Corp., Lectro Max Powder 100) powders in a glass vial [40].

The silicon-pitch cells were cycled in a voltage window of 5 mV - 1.5 V versus Li^+/Li, with one hour voltage holds at both the upper and lower voltage limits. This testing regime was designed to study the pitch matrix's ability to confine and withstand the full lithiation of the various silicon active materials. By calculating the approximate silicon content in each composite electrode, cycling currents were selected to achieve theoretical rates of C/20 (1^{st} cycle), C/10 (cycles 2-49) and C/5 (cycles 50-100) assuming 100% silicon utilization throughout testing.

Our sheet style electrodes were prepared by first gently mixing the appropriate ratio of tin (<150 nm, ≥99%, Sigma-Aldrich) or silicon (50 nm, 98%, Alfa Aesar) nanoparticles and polyacrylonitrile (PAN) powder (avg. M_w 150,000, Sigma-Aldrich) with a mortar and pestle. This homogenous mixture was then transferred to a screw-top glass vial where N,N-Dimethylformamide (DMF) solvent (Fischer) was added. After 12 hours of stirring with a magnetic stir bar, this vial was sonicated for another 6 hours to disperse any nanoparticles that may have agglomerated. This slurry was then evenly spread over the matte surface of a copper foil current collector using a 5 mm doctor blade. The resulting electrode sheet was immediately transferred to a 60°C oven for drying. With the DMF fully evaporated, 12 mm diameter punches were collected and subsequently heat-treated in a tube furnace at 270°C under continuous argon gas flow to cyclize the PAN binder. In the case of multi-layered electrodes, second and third layers of slurry were bladed atop of the first with 60°C drying steps between each application. The mass loading of active materials was found to be ~0.9 mg for Si-PAN electrodes and ~2mg for Sn-PAN electrodes. A traditional pressed powder pellet style electrode was prepared by hand mixing silicon, solid electrolyte powders and acetylene black in a 5:4:1 weight ratio. The active material mass loading of this electrode was ~1 mg after compaction.

To fabricate each cell, 150mg of the glassy solid electrolyte powders were pressed to 1 ton inside the Ti-PEEK die, forming a loosely compacted separator pellet. Punched sheet style electrodes or mixed composite electrode powders were then placed on one side of this pellet, with 50 mg InLi counter electrode powders on the opposing side. This assembly was then pressed to 5 tons for 5 minutes at room temperature in order to densify the separator layer and ensure good interfacial coupling between each layer.

All cells were cycled under constant current constant voltage (CCCV) conditions using an Arbin BT2000 battery tester at 60 °C. Cells were held at 60°C under 20 MPa compressive clamping force in a dry argon atmosphere. This small external compressive stress was applied to maintain good mechanical contact between the cells' electrodes and the cell die's titanium plungers. Each cell's first cycle was performed at a calculated C/20 rate. The following cycles were then conducted at a rate of C/10 unless otherwise stated. Pulse style internal resistance measurements were performed at the end of each charge and discharge. All cells containing tin were cycled in a voltage window of 5 mV - 1.5 V versus Li^+/Li, with a one-hour voltage hold at the upper voltage limit (CCCV) to ensure full de-lithiation of their anodes. The lower voltage limit was varied for the Si-PAN half-cells in order to investigate the effect on the anodes' capacity and capacity retention with cycling.

Rate studies were conducted on both Sn-PAN and Si-PAN sheet style electrodes in all-solid-state half cells utilizing InLi counter electrodes. These studies were carried out with charging (delithiation) rates ranging from 0.1C - 10C. The discharge (lithiation) rate was kept constant at 0.1C. For the Sn-PAN electrode, all cycles were conducted in a 5 mV - 1.5 V (vs. Li^+/Li) voltage window. The Si-PAN electrode underwent an initial conditioning cycle between 50 mV - 1 V at a C/20 rate. The following cycles were performed in a 100 mV - 1 V voltage window at various charging rates and a constant 0.1C discharge rate. All cycles, for both types of electrodes, were performed with constant current (CC) cycling parameters.

The microstructure of our electrodes was investigated via field emission scanning electron microscopy (FESEM, JEOL JSM-7401F) equipped with energy dispersive X-ray spectroscopy (EDS) capabilities. A dual-beam focused ion beam (FIB, FEI, Nova Nanolab 200) equipped with energy dispersive X-ray spectroscopy (EDS) was used to cross section and image electrodes and active materials both before and after inclusion into an ASSB.

The atomic structure of the electrode materials was characterized with a Bruker AXS D2 Phaser bench-top X-ray diffraction (XRD) system using Cu Kα radiation (λ=1.5418). Their impedance was measured with a Solartron 1280 Electrochemical Measurement Unit. Raman analysis of the electrodes was performed using a Horiba LabRAM HR Evolution Spectrometer with a 100 mW 532 nm frequency-doubled Nd:YAG laser source.

4 RESULTS AND DISCUSSION

4.1 Si-Ti-Ni Composite

STN composite electrodes with and without carbon black were electrochemically characterized vs. a lithium counter electrode. Figure 4 presents the cycling data for the 7:3 and 7:3:2 weight ratio composite electrode compositions of STN:SSE and STN:SSE:carbon black, respectively. It was found that the addition of carbon black dramatically improves cell reversibility. The STN electrode with carbon black achieves a 1st cycle discharge (delithiation) specific capacity of 483 mAh g^{-1} (electrode) and a 10th cycle discharge (delithiation) specific capacity of 405 mAh g^{-1} (electrode). These numbers correspond to an active material specific capacity of 828 and 695 mAh g^{-1} (active) for the 1st and 10th cycles, respectively. This same electrode also has a Coulombic efficiency that improves rapidly from 77.7% on the first cycle to 98.2% by the 10th cycle. The cell then failed with an internal short on the 15th cycle and no further data was recorded. Our previous liquid STN half cell exhibited a first cycle Coulombic efficiency of 87.7% [15]. The all-solid-state half cell has a lower Coulombic efficiency because the all-solid-state cell's comparatively larger amount of carbon black may have induced more side reactions during the initial charge cycle.

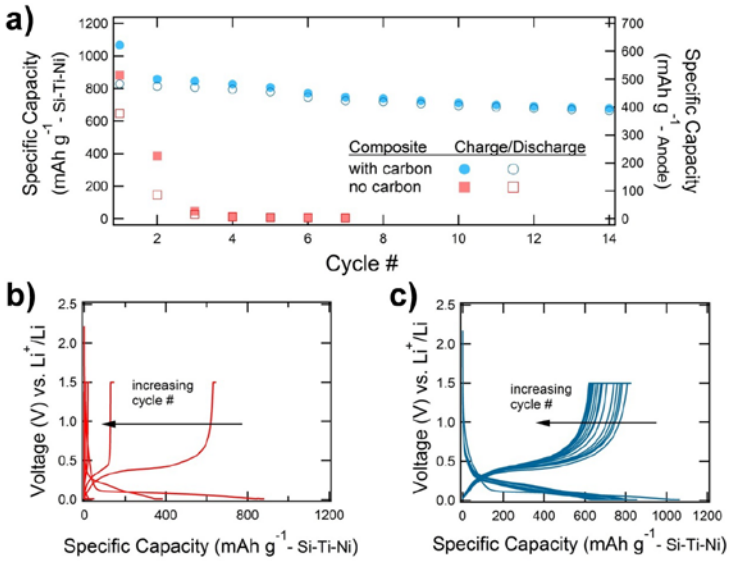

Figure 4. Cycling Stability and Voltage Profiles of STN Electrodes With (Blue) and Without Carbon Black (Red).

To explain why the addition of carbon black improves STN's cycling performance, the electronic conductivity of the STN matrix was tested before and after lithiation. Ionic conductivities of the STN matrix were previously measured [15]. The $Ti_4Ni_4Si_7$ matrix has a negligible ionic conductivity and an electronic conductivity of 10 S cm^{-1}. After electrochemical activation, the $Li_{3.2}Ti_4Ni_4Si_7$ matrix's ionic conductivity increases to 2.0 x 10^{-5} S cm^{-1} but its electronic conductivity decreases two orders of magnitude to 0.24 S cm^{-1}. The decrease in the matrix's electronic conductivity explains why the STN composite electrode without carbon black

could achieve a high initial capacity, but suffered from rapid capacity fade in subsequent cycles. Our previous studies with nano-Si required a nano-Si:SSE:conducting additive ratio of 1:5:1 [39, 41]. Because the $Li_xTi_4Ni_4Si_7$ matrix is a mixed conductor, the active material to carbon black mass ratio is increased from 1 to 3.5 and the active material to SSE mass ratio is increased from 0.2 to 2.33 over those previous studies.

Figure 5a presents the FESEM characterization of the uncompressed 7:3:2 weight ratio composite electrode powder. From this micrograph, it is evident that the composite electrode is comprised primarily of particles ranging from 1 to 6 microns in diameter. Figure 5b presents the elemental mappings for Si (red) and S (blue) overlaid on the accompanying FESEM micrograph. As expected, elemental mappings of Si and S are largely segregated to separate particles. Si rich particles are identified as STN particles, while S rich particles are identified as SSE particles. It is evident that the size of the STN particles is well matched to that of the sulfide glass SSE particles. Figure 5c presents the elemental mapping of C (green) overlaid on the same FESEM micrograph. We find that the carbon black particles are well dispersed throughout the composite electrode powder for good electronic transport to accommodate the decrease in the STN's electronic conductivity after the first cycle.

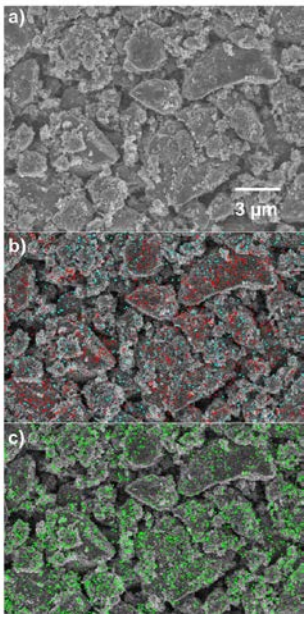

Figure 5. FESEM Micrographs of an Uncompressed STN Electrode

The next step of this study was to pair the optimized solid-state STN anode with a FeS_2 cathode. As a substitute for FeS_2, we instead utilized the recently developed mechanochemically prepared FeS + S composite active material [16] because all-solid-state electrodes made with this material can achieve higher overall specific capacities. The electrochemical characterization of an all-solid-state FeS + S/Li half cell cycled at 60°C is provided in Figure 6 as a reference to the reader. The FeS + S composite active material has the same theoretical capacity as FeS_2 but can be synthesized much more readily from inexpensive precursors. From Figure 6 it is observed that the capacity of a FeS + S composite electrode quickly exceeds its theoretical value of 900 mAh g^{-1} (active) or 281 mAh g^{-1} (electrode). Excess capacity is provided by the electrochemical activation

of inert Li_2S in the $77.5Li_2S{:}22.5P_2S_5$ glass electrolyte component of the composite electrode. The reversible electrochemical utilization of Li_2S in the SSE is facilitated by the good electronic conductivity of FeS as well as by the nano-size of FeS + S particles. The rise, fall, and stabilization of the electrode's capacity is associated with a complex electrochemistry where the reduction of FeS, S, and electrochemically precipitated FeS_2 phases all occur concurrently. After 60 cycles, the FeS + S composite electrode evolves a redox chemistry that is dominated by sulfur.

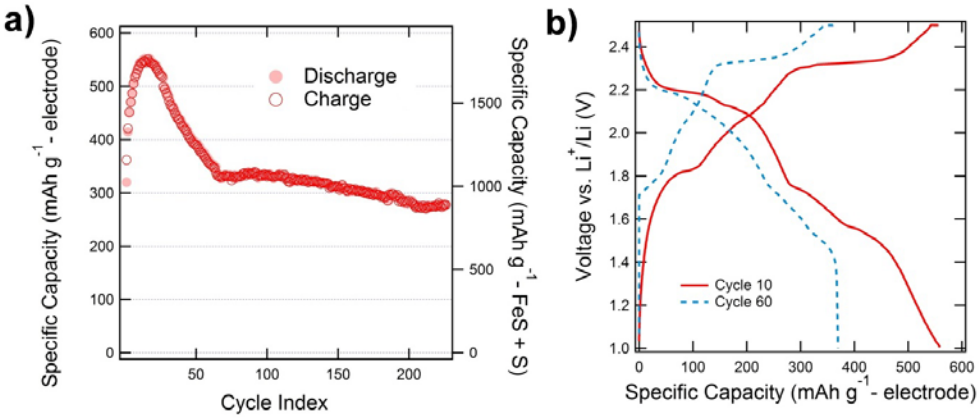

Figure 6. Cycling Stability and Voltage Profiles of a FeS+S/Li Half Cell

We adopted Jarvis et al.'s anode pre-lithiation technique [e] by incorporating SLMP into the uncompressed STN electrode powder (Figure 7a). During the cell's initial discharge the cathode is either lithiated by the direct oxidation of unreacted lithium metal or by the de-alloying of the pre-lithiated STN alloy. During subsequent cycles the cell behaves as a Li-ion battery. The cyclic stability of the FeS + S/STN full cell is given in Figure 7b. The cell achieves a 1st cycle specific discharge of 295 mAh g^{-1} (cathode) which corresponds to a FeS + S specific capacity of 944 mAh g^{-1} (active). This initial discharge capacity is close to the theoretical specific capacity of the FeS + S active material and it is consistent with previous results presented in Figure 6 [16]. As expected, the initial specific charge capacity rises dramatically to 383 mAh g^{-1} (cathode) and the discharge voltage plateaus centered at 1.6 V fade with extended cycling. Both of these results are also consistent with prior results. The increase in capacity is attributed to the electrochemical activation of excess Li_2S in the SSE component of the cathode [16, 42] and the fade of the lower voltage plateaus indicates that the sulfur redox chemistry comes to dominate the electrochemistry of the FeS + S cathode. The activation of excess Li_2S also explains why the full cell's initial discharge profile is different from that of subsequent discharge profiles.

From the voltage profiles of this cell (Figure 7c), it is confirmed that the full cell functions as a Li-ion cell and not as a lithium metal cell because the average discharge potential of the full cell is depressed compared to that of a FeS + S half cell [16]. The full cell also has a much more stable capacity compared to that of either the individual STN half cell (Figure 4c) or the FeS + S half cell (Figure 6). By the 100th cycle, the full cell maintains a specific discharge capacity of 355 mAh g^{-1} (cathode). When the mass of both composite electrodes are taken into account, the full cell delivers 225 mWh g^{-1} (anode + cathode) upon its 100th discharge.

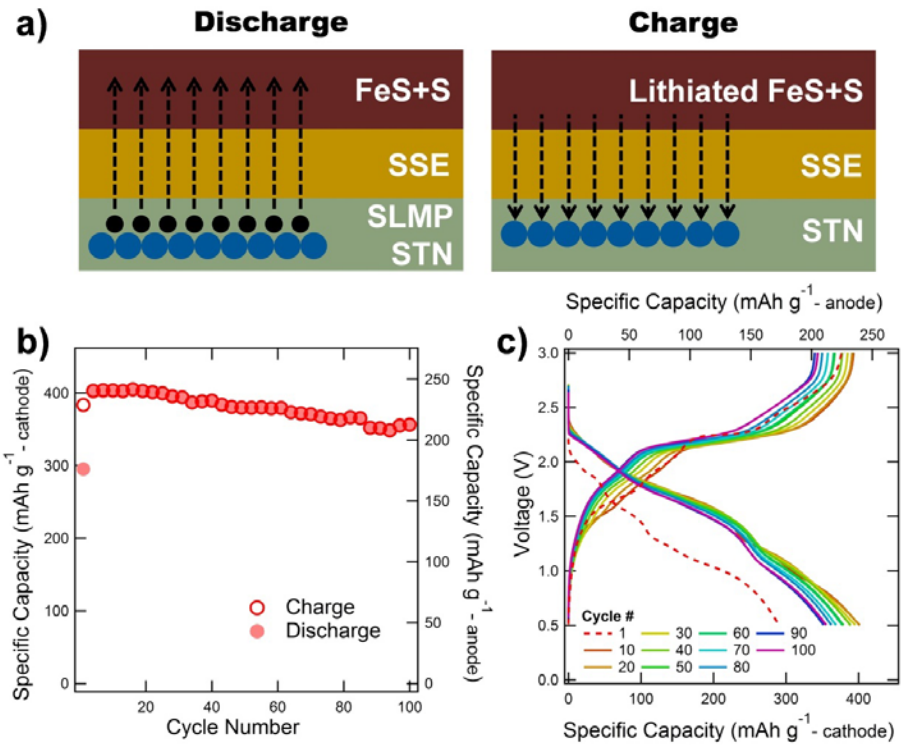

Figure 7. (a) Schematic of The Lithiation Mechanism (b) Cycling Stability and (c) Voltage Profiles of a Full Cell with a FeS + S Cathode and a Pre-Lithiated STN Anode

The FeS + S/Li and STN/Li half cells both behave much differently than the full cell. As discussed, the FeS + S/Li half cell's capacity dramatically rises, falls, and stabilizes, while the 7:3:2 composition STN/Li half cell looses 34% of its capacity between its 1st and 10th charge (lithiation) cycles. The stability of the full cell can be explained by considering three points. First, an excess of SLMP is added to the STN composite anode powder to offset inefficiencies and improve cyclic stability [18]. Second, the FeS + S cathode's complex electrochemistry is uniquely capable of offsetting the initial Coulombic inefficiency and fade of Si-based anodes. The characteristic rapid rise of the FeS + S cathode's capacity due to Li_2S activation in the SSE may help to offset losses from the STN anode. The result is a full cell with a stable capacity that does not rapidly rise like the FeS + S/Li half cell or initially fade like the STN/Li half cell. And third, the STN anode in the full cell was not fully utilized. From Figure 7b and c it is evident that the STN anode in the full cell never achieves a specific capacity in excess of 240 mAh g^{-1} (anode). This specific capacity should be revised because the mass of the anode in the full cell now considers the 1.35 mg of SLMP added to pre-lithiate the cell. For this reason, the specific capacity is revised to 286 mAh g^{-1} (anode) for accurate comparison with the 405 mAh g^{-1} (anode) achieved by the 7:3:2 STN/Li half cell during its 10th charge (lithiation). Limiting the depth of Si lithiation has been shown to improve the cyclic stability of other Si-based anodes [43]. By not fully utilizing the STN anode the same stabilization of capacity may be observed here as well. Incomplete utilization of the STN anode also suggests that further optimization of the full cell configuration may yield higher overall cell energy densities.

4.2 Silicon-Pitch Composites

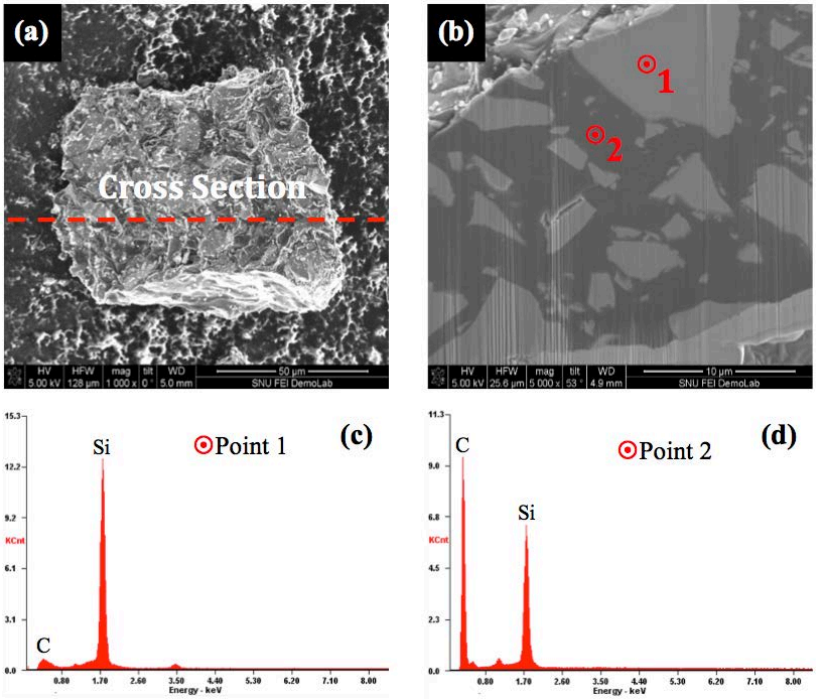

Figure 8. SEM Images and EDS Point Scan Spectra of a Heat-Treated Si-C Composite Particle Containing 325-Meshed Si-Particles

A Si-C composite particle prepared with 325 meshed (≤44 μm) silicon particles is displayed in Figure 8a. Although light colored silicon particles can be seen protruding through the dark carbon matrix, their distribution throughout the composite is unclear. To better understand the internal microstructure of this composite particle, it was cross sectioned and imaged with a FIB-SEM.

Figure 8b shows that despite the irregularity in their size and shape, the large silicon particles are evenly distributed and conformally encapsulated within the carbon matrix. The EDS data in Figures 8c and 8d confirm the composition of the light and dark phases identified by point scans one and two in Figure 8b. The small un-labeled peaks in Figures 8c and 8d indicate the presence of trace amounts of oxygen and gallium in the sample. These contaminants were likely introduced during the transport and FIB milling of the particle. Notice that a high degree of interfacial contact has been achieved between the carbon matrix and silicon particles. This conformal coating of the silicon active materials will help to prevent their electrochemical isolation with cycling. It will also facilitate the diffusion of Li-ions and electrons in and out of the silicon particles, as conduction in all-solid-state electrodes is typically limited to small particle-particle contact points rather than conformal interfaces. Lastly, this large degree of encapsulation may help to confine the volumetric expansion of the silicon particles upon lithiation, minimizing the stresses they experience with cycling.

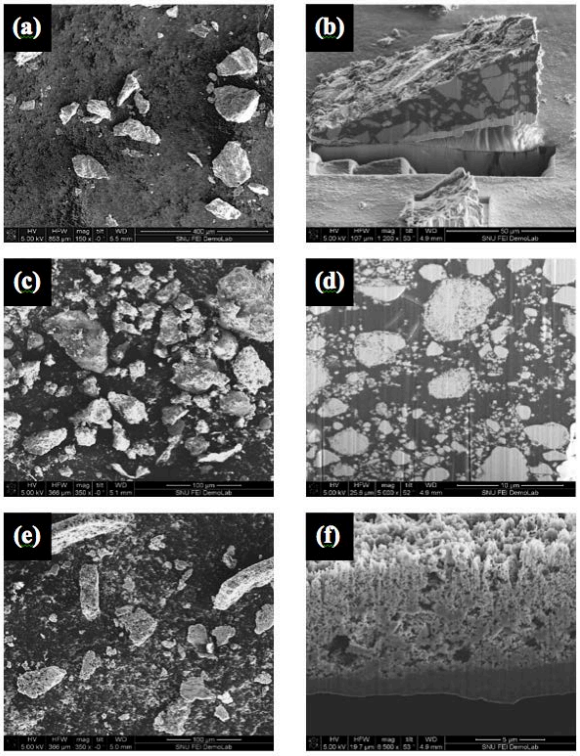

Figure 9. S EM Images of Heat-Treated Si-C Composites Containing 325-Meshed [≤44 μm] (a,b), 1-3 μm (c,d) and 50 nm (e,f) Si-Particles

The variation in size and morphology of the Si-C composite particles after heat treatment and hand grinding is shown in Figures 9a, 9c and 9e. The composite particles range in size from tens to hundreds of microns in diameter. These low magnification scanning electron microscope (SEM) images show that the heat-treated composites are tough enough to withstand the stresses of hand grinding without crumbling or phase separation. This suggests that the benefits of the conformal Si-C composite structure will be maintained in an all-solid-state electrode.

SEM images of cross-sectioned Si-C composite particles are displayed in Figures 9b, 9d and 9f. The large 325-meshed (≤44 μm) silicon particles in Figure 9b are evenly dispersed and conformally encapsulated in a dark, dense carbon matrix. The smaller 1-3 μm present in Figure 9d also clearly show a high degree of interfacial contact with its surrounding carbon matrix, although some silicon particle agglomeration can be observed in this particular cross section. The composite prepared with 50 nm silicon particles has a slightly different morphology. At this magnification, this Si-C composite clearly shows porosity not present in the other cross-sectioned anode particles. This is due to the large surface area of the silicon nano-particles, around which the pitch carbon must coat. The robustness of these composite particles shows that their active silicon nano-particles are strongly bound together by their carbon matrix, despite any visible porosity. This conformal binder like coating will help to hold the silicon nanoparticles together, linking them in a three-dimensional conducting network.

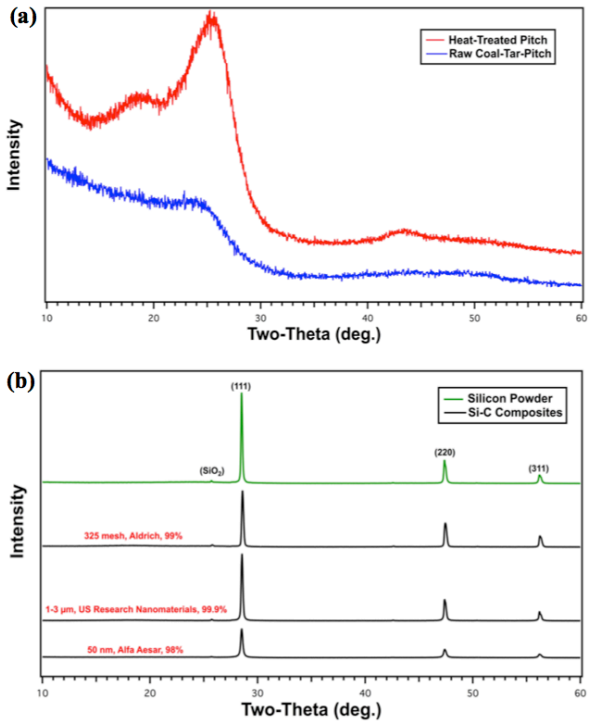

Figure 10. XRD Patterns of Coal-Tar-Pitch Powders and Si-C Composite Particles

X-ray diffraction (XRD) patterns of the coal-tar-pitch before and after heat treatment are plotted in Figure 10a. Before heat-treating, pitch is composed of complex arrangements of mostly planar polycyclic aromatic hydrocarbons with wildly varying molecular weights and configurations [44]. The broad, low intensity peaks of the unprocessed pitch are characteristic of the amorphous nature of this extremely complex industrial waste material. Upon heating, pitches soften into a relatively low viscosity liquid, making them ideal candidates for the formation of particle-matrix style composite materials. This liquid, or mesophase, allows the pitch's volatile low molecular weight components to distill while the larger ring compounds polymerize into planar aromatic structures [20]. Further heating results in the coalescence and alignment of these planar structures into parallel stacks similar to graphite. This ordering of the heat-treated pitch can be verified by the increased intensity and angle of its diffraction peaks. These peaks, observed around 25° and 43°, represent the (002) and (100) diffraction modes, respectively, and while their increased intensity suggests decreased d-spacing in the material, their broadness is proof that the heat-treated pitch lacks any long-range repeating order and thus remains amorphous.

Figure 10b compiles XRD patterns of the heat-treated Si-C composite powders along with a baseline scan of pure 1-3 µm silicon powder for reference. The sharp (111), (220) and (311) crystalline peaks of the silicon powder, shown in green, match the literature [45]. A small peak around 26° suggests that the silicon particles have at their surface a thin, partially crystalline, native oxide layer. This is not uncommon for silicon stored outside of a dry glovebox [21,46,47,48]. The similarity of the silicon powder baseline scan to the profiles of the Si-C composite powders further demonstrates the amorphous structure of the carbon matrix material. The absence of any unexpected peaks also shows that no secondary crystalline phases formed between the silicon and carbon, or any undetected impurities, during the heat-treatment process.

To investigate the electrochemical activity of the heat-treated coal-tar-pitch, an all-solid-state half-cell was prepared with a 2 mg heat-treated pitch working electrode. This pitch received the same heat treatment as the other Si-C composite particles presented in this report. The cycling performance of this cell is shown in Figure 11a, with select voltage profiles and dQ/dV plots displayed in Figures 11b & 11c, respectively. This pure pitch electrode achieved a large first cycle specific lithiation capacity of 964.1 mAh/g, but only 621.28 mAh/g of this capacity was reversible. This corresponds to a first cycle coulombic efficiency of only 64.4%. These capacities are far greater than the theoretical limit of graphite intercalation (~372 mAh/g), but this is not unprecedented for soft carbon materials [21,49,50,51,52].

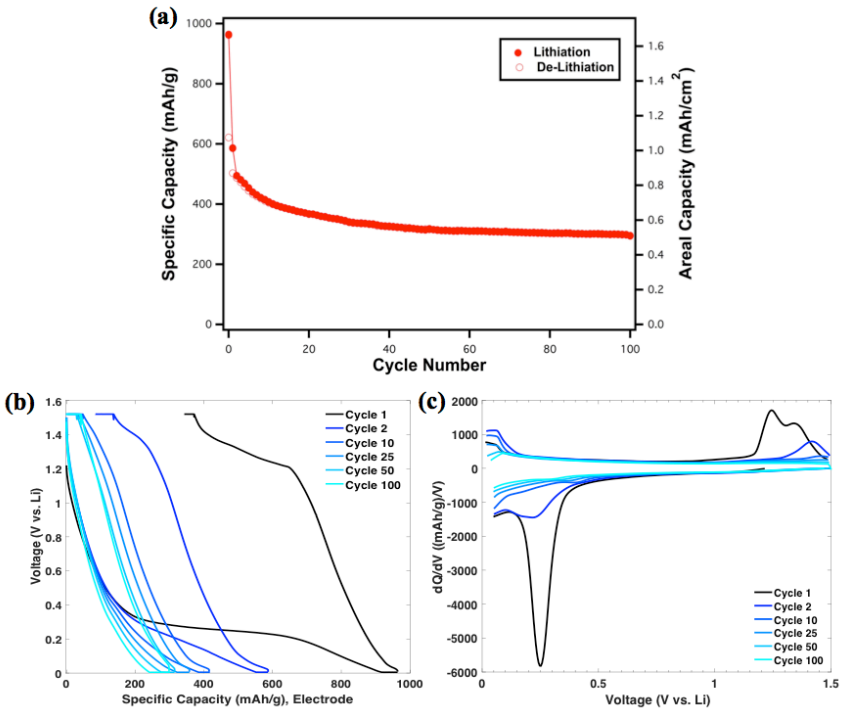

Figure 11. (a) Cycling Performance (b) Voltage Profiles and (c) dQ/dV Plots of a Pure Heat-Treated Pitch Electrode in an All-Solid-State Li-Ion Half Cell

Much of this pitch electrode's large first cycle capacity can be attributed to lithiation and de-lithiation plateaus centered around 0.25 V and 1.25 V, respectively. While similar voltage profiles have been reported for other pitch based soft carbons, the physical interpretation of these large plateaus remains somewhat of a mystery. Larcher et al. suggested that some of the initial discharge capacity could be attributed to irreversible reactions with undetected elemental oxygen and sulfur in the heat-treated pitch [49,53]. On the other hand, Zheng et al. convincingly argued that these high voltage plateaus were the result of lithium atoms semi-reversibly binding in the vicinity of hydrogen atoms in the soft carbon, showing that the presence and magnitude of these large voltage plateaus scaled directly with the hydrogen content of the pyrolyzed organic material tested [50,51,52]. We believe that a combination of these two mechanisms is responsible for this electrode's relatively large semi-reversible initial capacity.

The large voltage plateaus that greatly contributed to the pitch electrode's initial capacity and hysteresis had nearly vanished after 10 cycles, leaving behind a gentle sloping voltage profile with a coulombic efficiency >99%. The disappearance of these plateaus was likely due to both the irreversibility of their underlying reactions and the development of a large overpotential. This overpotential can be attributed to the disruption of conduction pathways through the all-solid-state electrode. The utilization of a conductive binder or additive such as SSE would likely have reduced the magnitude of this overpotential and improved the electrode's capacity retention with cycling by improving and maintaining interfacial contact between the active particles.

Despite containing no SSE, this heat-treated pitch electrode maintained a stable 100th cycle discharge capacity of over 300 mAh/g with a 100% coulombic efficiency at a 0.38 mA/cm^2 current density. The 100th cycle's sloping voltage profile is characteristic of lithium ions partially charge transferring to the surface of planar aromatic structures present in the soft carbon material [54]. A low voltage plateau, resulting from the one-hour lower limit voltage hold, suggests that stack intercalation and reversible lithium plating may have also contributed to the electrode's capacity. Not only was this electrode able to achieve a 100th cycle specific capacity in the range of the theoretical limit of graphite, it was able to do so without the addition of any conducting additives. This result is important because it shows that even at large current densities, heat-treated coal-tar-pitch can cycle on its own by simultaneously acting as both active material and ionically/electronically conductive additive in an all-solid-state electrode. Therefore, by coating silicon particles in this mixed conducting electrochemically active carbon, we can reduce or even eliminate the need for inactive additives such as carbon black in our all-solid-state electrodes, increasing their volumetric and gravimetric specific capacities.

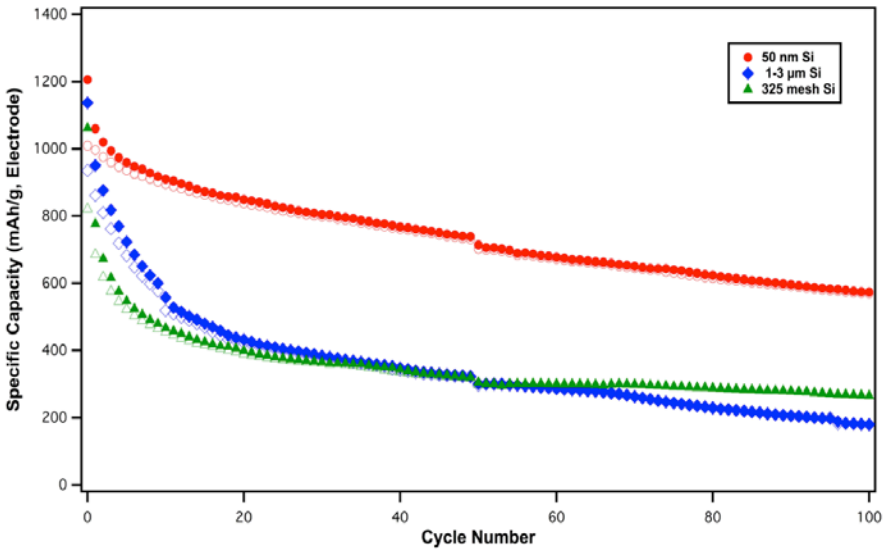

Figure 12. Cycling Performance of All-Solid-State Li-Ion Half-Cells Made With 7:3 Si-C:SSE Working Electrodes Containing Various Sizes of Silicon Particles

In order to investigate the heat-treated pitch's effectiveness as a rigid matrix, three different composite anode materials were prepared with varying sizes of silicon active particles. Much of the literature on silicon anodes has depended on the superior cycling stability of complex

nanostructured active materials. By testing a variety of silicon powders, we hoped to investigate this pitch matrix material's ability to enable the stable cycling of inexpensive and more readily available silicon micro-particles. To test the effectiveness of these composite anode materials, three identical all-solid-state half-cells were prepared. Each cell was prepared in the same fashion, but utilized silicon particles of different size (50 nm, 1-3 μm or 325 meshed). These cells contained 2 mg 7:3 Si-C:SSE working electrodes, corresponding to Si-C composite and silicon particle mass loadings of approximately 1.4 mg and 0.7 mg, respectively. This experiment will be referred to as the particle-size study.

The cycling performance of the three particle-size study cells is plotted in Figure 12. Note that the capacities are all normalized to the total electrode mass, not per gram of active material. From looking at Figure 12, it is clear that the composite anode made with 50 nm silicon particles (red) outperformed the two composites containing micron-sized silicon particles in first cycle capacity, coulombic efficiency and capacity retention. This result was expected, as nano-structured silicon active materials are known to outperform larger silicon particles due to their decreased diffusion distances and facile stress relaxation upon lithiation [55,56]. The goal of this experiment was to determine if the mixed conducting coal-tar-pitch derived carbon was robust enough to enable the deep lithiation of large silicon micro-particles in an all-solid-state LIB. By encapsulating the silicon active materials in an amorphous carbon matrix, we hoped to restrict their volumetric expansion and limit their pulverization with cycling. Unfortunately, this data suggests that the amorphous carbon was not robust enough to withstand the extreme volumetric expansion of these large silicon micro-particles upon deep discharge to 5 mV and could not prevent the irreversible capacity losses brought on by their electrochemical isolation with cycling.

Figures 13 (a-f) show select voltage profiles and dQ/dV plots for the three cells included in this particle-size study. The first cycle voltage profile for all three cells has a long flat lithiation plateau around 0.13 V. Shown as a single sharp cathodic peak in the dQ/dV plots, this low voltage lithiation plateau represents the well documented two phase conversion of crystalline silicon into amorphous Li_xSi phases [57]. It is interesting that the first cycle cathodic peak observed around 0.25 V in the 100% heat-treated pitch electrode cannot be clearly seen in any of the cells in Figure 13, although the pitch delithiation peak ~0.07 V is faintly present. This makes it difficult to determine the extent to which the amorphous carbon matrix material is lithiated and how much it contributes to the overall capacity of the electrodes with cycling. Because of this, the specific capacities in this report will be normalized to total electrode mass or total mass of active composite, not per gram of silicon or pitch individually.

With cycling, the particle-size study cells' voltage profiles steadily retract while becoming increasingly sloping in nature. In the dQ/dV plots, two broad lithiation peaks can be observed in the second cycle of all three cells. These two peaks, centered around 0.24 V and 0.07 V, are characteristic of single-phase transitions between the various amorphous Li_xSi phases [57,58]. As cycling progressed, the intensity of these broad cathodic peaks slowly decreased as they shifted to slightly lower voltages. This decrease in peak height represents the electrochemical isolation of active silicon particles while the shift, or overpotential, is the result of increasing electrode resistance due to pulverization of its mixed conducting composite microstructure.

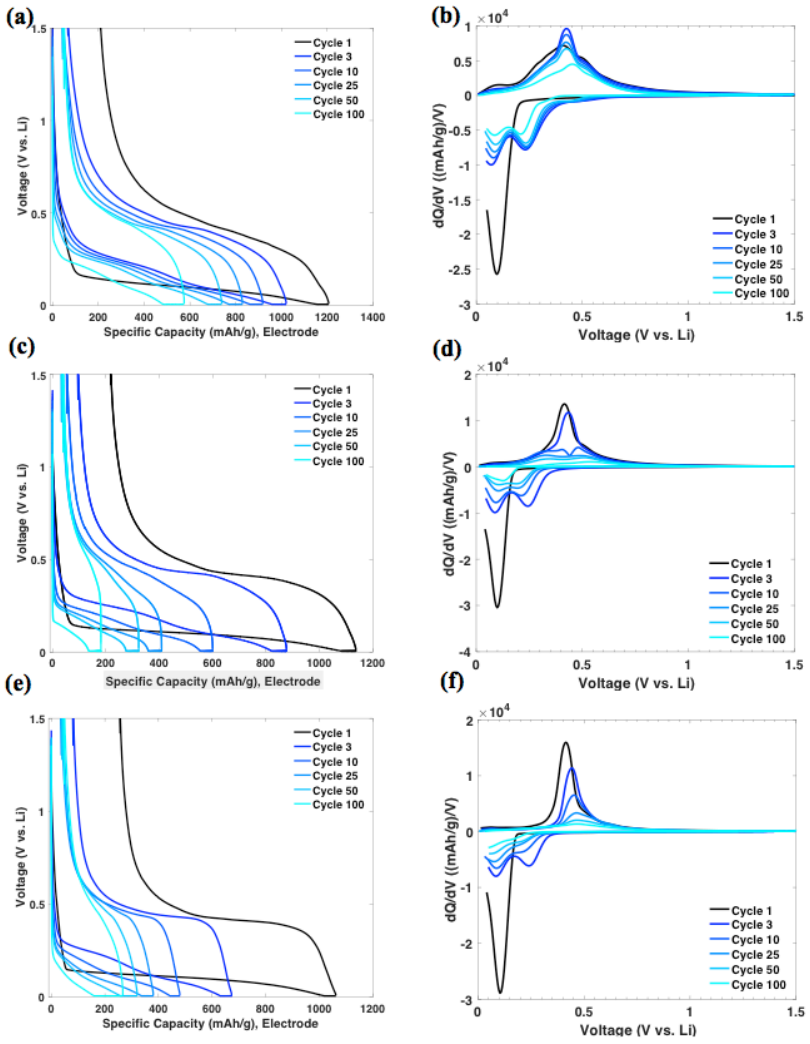

Fig ure 13. Voltage Profiles and dQ/dV Plots of 7:3 Si-C:SSE All-Solid-State Half Cells Prepared with 50 nm (a,b) 1-3 µm (c,d) and 325 Meshed (e,f) Si-Particles

All three cells show a sharp delithiation peak centered ~0.42 V. This anodic peak represents a two-phase transition in which the fully lithiated $Li_{15}Si_4$ crystal converts back to delithiated amorphous silicon. The presence of this sharp anodic peak (a-$Li_{15}Si_4$) is a clear indication that the $Li_{15}Si_4$ metastable crystal structure nucleated in the electrodes' silicon particles during their deep discharge to 5 mV. This a-$Li_{15}Si_4$ peak is initially present in Figures 13d & 13f, but quickly shrinks into a broad hump more akin to the delithiation of amorphous silicon phases with continued cycling. The disappearance of the a-$Li_{15}Si_4$ peak shows that while the saturated $Li_{15}Si_4$ crystalline phase initially nucleated in these large silicon micro-particles, it became unfavorable with continued cycling. This can be attributed to an increasing overpotential in the pulverized electrodes shifting the crystallization potential outside of the applied voltage window. In other words, the electrode's fragmented microstructure introduced so much resistance to the system that the applied current quickly resulted in polarization and heat loss rather than electrochemical work. This polarization led to a slowing of the electrochemical reaction rate and greatly limited the silicon active materials' degree of lithiation.

The broad first cycle delithiation curve in Figure 13b can be interpreted as a combination of the two peaks associated with transitions between the amorphous Li_xSi phases (0.3 V & 0.49 V) and the sharp anodic peak (a-$Li_{15}Si_4$) representing the two-phase delithiation of the $Li_{15}Si_4$ crystal structure. The presence of both crystalline and amorphous silicon dQ/dV peaks shows that despite being potentiostatically held at 5 mV, some silicon nano-particles were unable to nucleate the $Li_{15}Si_4$ crystal. This is proof that the pitch matrix was robust enough to limit the free volume expansion of some of its encapsulated silicon nano-particles, preventing them from fully lithiating and thus suppressing their crystallization. A small but consistent overpotential in the cell's initial lithiation peaks is consistent with this confinement of the silicon particles [59]. Because this overpotential remains relatively steady with cycling, we can confidently conclude that the continued suppression of the silicon nano-particles' full lithiation is not due to degradation of mechanical contacts in the electrode but is solely related to their confinement in a rigid amorphous carbon matrix. And while similar results have been reported for all-solid-state electrodes cycled under large externally applied compressive stresses, our data shows that confining forces can be achieved in situ by the encapsulation of silicon nano-particles in a mixed conducting amorphous carbon matrix [59]. This is highly desirable because the application of large external compressive stresses is not practical for future commercialization of the all-solid-state LIB.

Large internal stresses develop at the interface between amorphous silicon and the saturated $Li_{15}Si_4$ crystal phase. These large stresses can lead to the fracture and electrochemical isolation of silicon active materials during cycling. By confining their expansion below the threshold for forming the $Li_{15}Si_4$ crystal, the rigid amorphous carbon matrix helped to limit the stress in the silicon nano-particles. This limitation of the silicon particle expansion results in reduced capacity, but it improves cycling stability, an important metric when transitioning to full cell configurations. While similar lithiation restrictions can be achieved by simply limiting the lower voltage limit of the cell, we were interested in investigating the pitch matrix's ability to apply confining forces on the silicon particles in situ. The deep discharge of the active materials was therefore used as a test of the amorphous carbon matrix material's ability to confine and withstand the expansion of various silicon particles, as any restriction to free volume expansion in this cycling regime would certainly translate to improved cycling stability at lower degrees of lithiation.

It should be mentioned that no crystallization suppression was observed in the silicon micro-particle composite electrodes' initial dQ/dV charge profiles, as only the sharp a-$Li_{15}Si_4$ peak could be observed. Had the lithiation of any of the active silicon micro-particles been limited to levels below the threshold for forming the $Li_{15}Si_4$ crystal, we would expect to observe a broad anodic dQ/dV profile as in Figure 13b. This shows that the pitch carbon coating was not robust enough to restrain the free volume expansion of the large silicon particles, pulverizing instead. Unfortunately, these results suggest that the pitch derived amorphous carbon matrix is not effective in enabling the long-term utilization of inexpensive silicon micro-particles in a rechargeable all-solid-state LIB. While reduction of silicon mass loading in the composite, limiting the lower voltage limit and removal of the low voltage hold would surly improve the cycling stability of these all-solid-state electrodes, this optimization is left for future work. The remainder of this paper will instead focus on the effect of SSE content on the composite electrodes' cycling stability.

In order to demonstrate the full potential of the heat-treated coal-tar-pitch matrix material, a series of all-solid-state half-cells was constructed utilizing the Si-C active composite prepared with 50 nm silicon particles. The five cells in this study were assembled with electrode composite ratios (nSi-C:SSE) ranging from 6:4 to 100% Si-C (no SSE added to the working electrode). By varying the amount of SSE in the cells' electrodes, an optimum balance between electrode specific capacity and capacity retention with cycling was to be discovered. This experiment will be referred to as the electrode-composite study.

The cycling capacities of the electrode-composite study half-cells are plotted in Figure 14. Notice that the cells' initial specific lithiation capacity scales directly with the mass fraction of active Si-C particles in their composite electrodes. This is because these specific capacities are calculated per gram of electrode, not per gram of active material in the electrodes. Figure 14 shows that the cycling stability of these cells generally increases with the mass fraction of SSE in their working electrodes. For example, while the 100% Si-C cell achieved the largest first cycle specific lithiation capacity (2082.8 mAh/g) of any cell tested, its capacity quickly decreased to 506.3 mAh/g after only 25 discharge-charge cycles. On the other hand, the 6:4 Si-C:SSE composite working electrode, which had the smallest first cycle specific lithiation capacity (1115.2 mAh/g), experienced relatively little capacity loss with cycling and finished 100 discharge-charge cycles with the highest capacity of any cell in this study (653.5 mAh/g at a 0.38 mA/cm^2 current density). Normalizing this cell's 1^{st} and 100^{th} cycle capacities to mass of active Si-C composite results in specific lithiation capacities of 1858.7 mAh/g and 1089.2 mAh/g, respectively. This corresponds to 1^{st} and 100^{th} cycle areal capacities of 1.66 mAh/cm^2 and 0.97 mAh/cm^2. Therefore, not only does this half-cell outperform all others in this study, it also exceeds the capacity reported for a similar material cycled in a traditional coin cell configuration after 100 cycles [21].

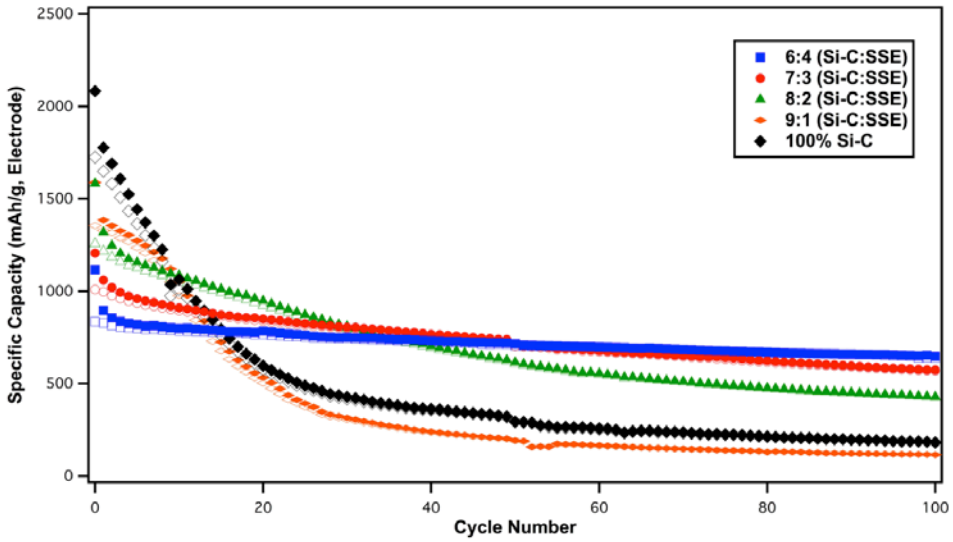

Figure 14. Cycling Stability of All-Solid-State Li-Ion Half Cells Containing nSi-C:SSE Composite Working Electrodes of Various Compositions

All five cells in Figure 14 displayed first cycle coulombic efficiencies around 83%, regardless of SSE content in their composite electrodes. Similarly, all of the cells displayed second cycle efficiencies of ~92%. These low coulombic efficiencies can be attributed to initial electrochemical isolation of active materials and irreversible reactions in the all-solid-state electrodes. With continued cycling, the coulombic efficiencies of these five cells diverged and a trend became clear. The cells that contained more solid electrolyte achieved and maintained coulombic efficiencies >99% earlier. For example, the 6:4 Si-C:SSE composite working electrode achieved a stable >99% coulombic efficiency after less than 20 cycles, while it took the 8:2 Si-C:SSE electrode ~50 cycles and the 100% Si-C electrode nearly 90 cycles to achieve the same. This shows that the added SSE improves the reversible utilization of the Si-C active materials in an all-solid-state electrode, leading to improved capacity retention with cycling. This can be attributed to the additional SSE improving interfacial contact with the active Si-C composite particles, reducing their likelihood of isolation upon delithiation. It also shows that additional SSE does not lead to continual development of fragile solid-electrolyte-interphase layers that can limit the coulombic efficiency of conventional cells utilizing liquid based electrolytes.

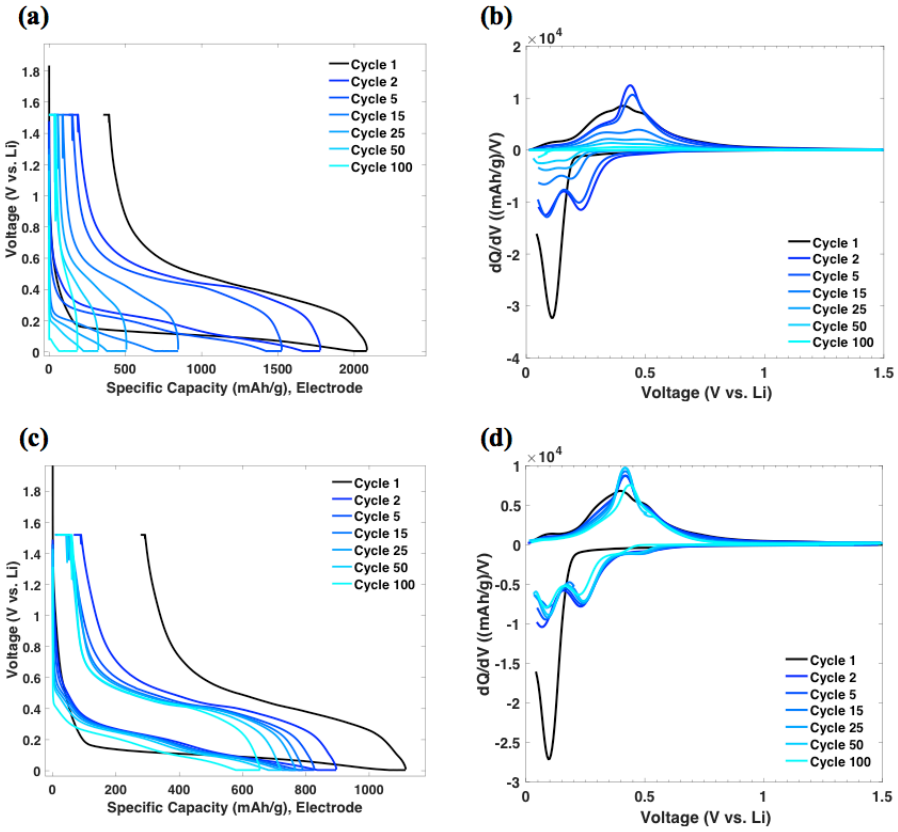

Figure 15. Voltage Profiles and dQ/dV Plots for Two All-Solid-State Half-Cells Utilizing 50 nm Silicon Particles in Their Working Electrodes (a,b) Represent a 100% nSi-C Electrode While (c,d) Represent a 6:4 nSi-C:SSE Composite Electrode

The voltage profiles and dQ/dV plots for the 100% Si-C and 6:4 Si-C:SSE electrodes are presented in Figures 15 (a-d). These plots display the characteristic silicon lithiation plateaus and peaks discussed earlier with no signs of any unexpected side reactions. The similarity of both cells' first cycle voltage profiles shows that the Si-C composite material does not require the addition of SSE to cycle in an all-solid-state cell. This is further proof of the facile mixed conductivity of the amorphous carbon matrix material.

A large overpotential quickly developed in the 100% Si-C electrode. This resulted in the disappearance of the sharp a-$Li_{15}Si_4$ peak after only 5 cycles. The 6:4 Si-C:SSE electrode experienced virtually no voltage shift, so rather than disappearing, its a-$Li_{15}Si_4$ peak actually increased in magnitude over its first 50 cycles. Growth of the a-$Li_{15}Si_4$ peak can be attributed to decreased confinement of the silicon active particles leading to an increase in their free volume expansion upon lithiation. This reduction of silicon particle confinement may be explained by gradual fracturing of the Si-C composite as well as inelastic deformation of the surrounding SSE matrix with cycling. While a small increase in a-$Li_{15}Si_4$ peak height was observed for this cell, the capacity of the electrode remained remarkably stable suggesting that continued damage to its composite microstructure with cycling was minimal.

The exceptional stability of the 6:4 Si-C:SSE electrode's dQ/dV plots suggests that the growing overpotential in the 100% Si-C electrode can be attributed to the fragmentation and disruption of interfacial contacts between its composite particles. The presence of SSE in the electrode clearly improves the cycling stability of the Si-C composites. This is because the SSE behaves as a secondary ionically conductive matrix, improving interfacial contact between the active Si-C composite particles much in the same way that the pitch derived amorphous carbon encapsulates and confines the silicon nano-particles. Increasing the mass loading of SSE in the composite electrode allows for more conformal coating of the electrochemically active Si-C particles. This ensures improved interfaces and connectivity in an electrode that would otherwise be limited to particle-particle contact points between relatively brittle active materials.

No clear peaks corresponding to the lithiation or delithiation of the coal-tar-pitch derived amorphous carbon matrix can be observed in either cells' dQ/dV plots. Because of this, it is difficult to make any confident conclusions on the extent of soft carbon utilization in these cells. While these electrodes' capacities could theoretically be attributed to their silicon particles alone, we believe it is highly unlikely that the amorphous carbon matrix remained inactive. For example, the 6:4 Si-C:SSE electrode had a total mass of 1.98 mg, corresponding to about 1.188 mg of Si-C composite particles or around 0.7128 mg of silicon and 0.4752 mg of amorphous carbon. Assigning conservative specific capacity values of 3000 mAh/g and 300 mAh/g to the silicon and carbon phases would result in first cycle specific capacities of ~ 1152 mAh/g (electrode) and 1920 mAh/g (active material). These values vary from those actually observed for the cell by only 3%. When applied to the 100% Si-C electrode, this calculation predicts a first cycle specific lithiation capacity 7% smaller than what was observed experimentally. This shows that the Si-C composite materials were able to achieve high degrees of silicon and carbon utilization without the aid of the ionically conductive additives, and that the addition of SSE primarily helped with maintaining interfacial contact throughout the working electrode.

After 100 cycles, select electrodes were cross-sectioned and imaged with a FIB-SEM system. Figure 16a shows the internal microstructure of the 6:4 Si-C:SSE electrode prepared with 50 nm silicon particles. Notice that this electrode is almost totally dense with very little cracking or porosity. This cell maintained a stable capacity throughout cycling because it contained enough malleable SSE to extensively link its electrochemically active Si-C composite

particles in an ionically conductive matrix. Maintaining a high degree of interfacial contact between the composite particles is critical to preventing active material isolation in all-solid-state cells where conduction pathways are limited to small, particle-particle contact points. These bottleneck points restrict the movement of Li-ions through the cell and can be easily disrupted during cycling leading to irreversible capacity losses.

Compare Figure 16a to the cross-section of the 7:3 Si-C:SSE electrode prepared with the same 50 nm silicon composite anode material (Figure 16b). Large voids can clearly be seen permeating through the 7:3 Si-C:SSE electrode. Since the same Si-C composite material was used in both cells, the presence of these large voids must therefore be attributed to the lower mass loading of SSE in the electrode. These voids or separated interfaces are detrimental to the electrochemical performance of the cell because they act as roadblocks to electrons and Li-ions traveling through the electrode, increasing resistance. Furthermore, these voids allow for the free volume expansion of surrounding active materials, enabling their fracture and isolation with cycling.

The relationship between electrode porosity, pulverization and capacity fade with cycling is further highlighted by the cross-sectioned 7:3 Si-C:SSE electrode presented in Figure 16c. This cell, which was prepared with larger 1-3 μm silicon particles, displayed the poorest cycling performance of any tested in this study (Figure 12). The cross sectional image of this electrode shows a high degree of cracking and delamination at the interfaces between the SSE matrix and the Si-C composite particles. This delamination was likely exacerbated by the free volumetric expansion of the large silicon micro-particles. Therefore, by failing to maintain interfacial contact with the active composite materials and restrain their volumetric expansion, these voids accelerated the electrode's irreversible capacity losses with cycling. In the future, we will investigate alternate processing methods to further improve interfacial connectivity in these all-solid-state electrodes, increasing the cycling stability and utilization of the Si-C composite anode materials.

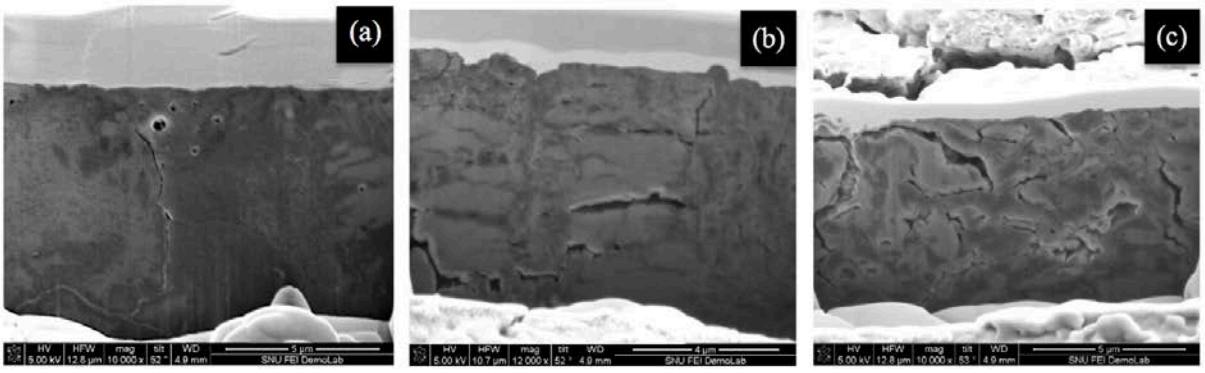

Figure 16. FIB Cross Sectional Views of Si-C:SSE Composite Electrodes After 100 Charge-Discharge Cycles, (a) 6:4 nSi-C:SSE Composite Electrode, (b) 7:3 nSi-C:SSE Composite Electrode, and (c) 7:3 Si-C:SSE Composite Electrode Containing 1-3 μm Silicon Particles

4.3 Polyacrylonitrile Enabled Slurry Coated Sheet Style Electrodes

To follow up on our previous success with tin based pressed pellet style electrodes, we decided to investigate the nano-tin particles as active materials for slurry coated sheet style anodes in ASSBs. This next section of the report describes our work on the optimization of these Sn-PAN electrodes.

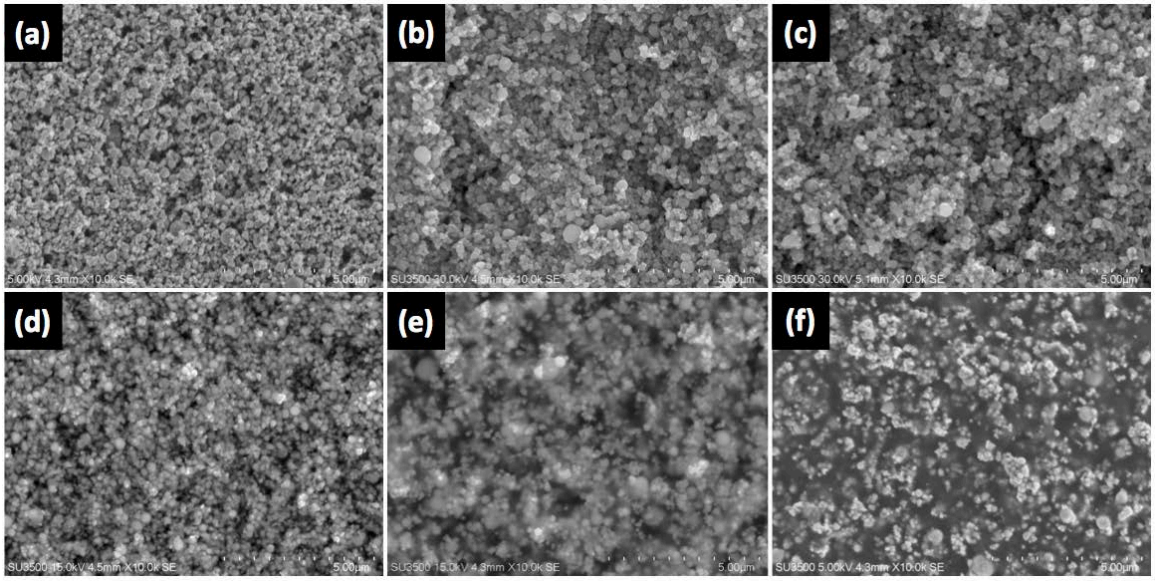

Figure 17. 10,000x SEM Images of Heat-Treated Sn-PAN Electrodes with (a) 0%, (b) 2.5%, (c) 5%, (d) 10%, (e) 20%, (f) 30% Binder Content

Figure 17 shows the surface morphology of various heat-treated Sn-PAN electrodes. Notice that the tin nanoparticles in the binder-free electrode (Figure 17a), prepared by blading a suspension of tin nanoparticles and DMF over a copper foil current collector and drying, remain spherical and well dispersed despite being heated above their melting point. The electrode containing 2.5% PAN (Figure 17b) has a porous structure similar to the uncoated electrode with little observable aggregation. This suggests that the small mass loading of binder, only ~6% of the electrode's total volume, is not enough to fully encapsulate the tin nanoparticles. The binder coating becomes more evident in the 5% PAN electrode (Figure 17c) as the volume fraction of binder increases to 24.5%. A subtle disappearance of small pores between neighboring tin nanoparticles alludes to a more conformal PAN network in this electrode. Although the PAN more completely encapsulates the tin active materials, individual nanoparticles are still clearly defined at this relatively low magnification. This suggests that the binder coating remains reasonably thin. The binder becomes more noticeably thicker in the subsequent images, as the weight percent of PAN in the electrodes grows from 10-30%. As the mass loading of PAN increases, the SEM images become darker with a shallower depth of field. This can be attributed to the relatively resistive PAN more completely filling the pore spaces in the electrode. Figure 17f shows this clearly, as only a few bright tin nanoparticles can be seen protruding from the dark, dense PAN matrix that makes up >70% of the electrode's total volume.

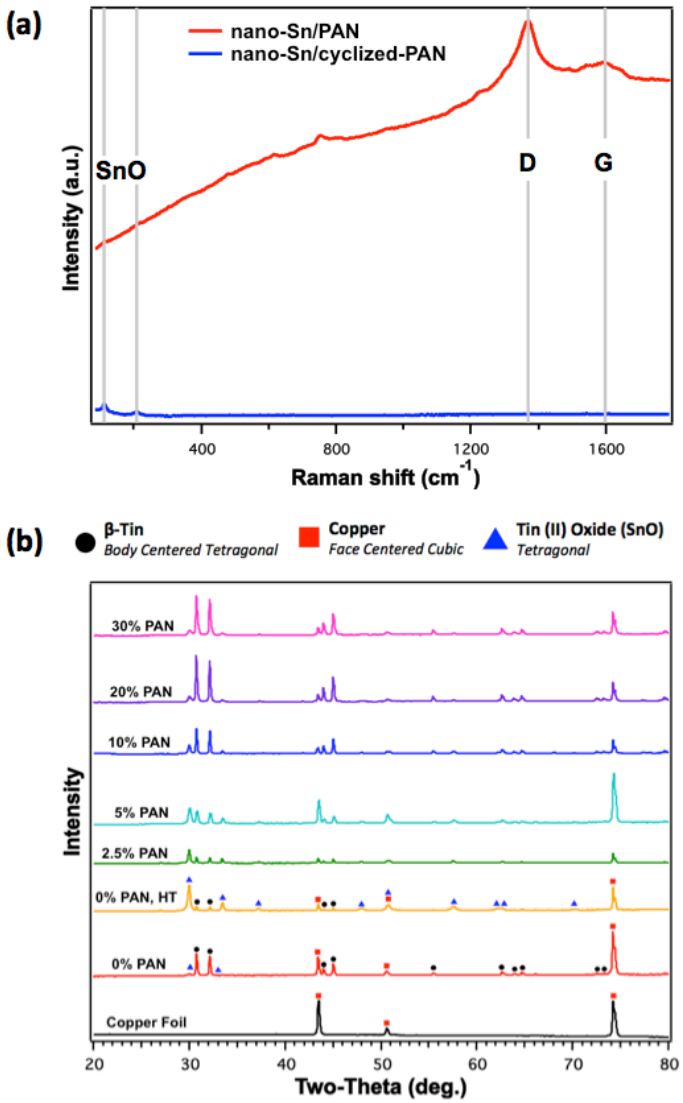

Figure 18. (a) Raman Spectra of a Slurry-Coated nSn-PAN Electrode (95:5 - nSn:PAN) Before (Blue) and After (Red) Heat Treatment (3hrs - 270°C - Ar) (b) XRD Spectra of Various Heat-Treated Sn-PAN Electrodes Along With a Non Heat-Treated 100% nSn Sheet-Style Electrode and an Uncoated Copper Foil Current Collector for Reference

To experimentally confirm the stabilization of the PAN binder, we used Raman spectroscopy to characterize a 5% PAN electrode before and after heat treatment (Figure 18a). The spectrum of the untreated electrode (blue profile) shows two faint Raman shifts at 110 cm^{-1} and 210 cm^{-1}. These shifts indicate the presence of native SnO in the untreated slurry-coated electrode [60]. No peaks associated with tin were observed, as pure metals display no Raman shifts. The spectrum of the same electrode after heat treatment (red profile) contains two new prominent shifts at 1350 cm^{-1} and 1580 cm^{-1}. These shifts are attributed to the D and G bands characteristic of delocalized sp^2 π bonding, respectively [34,61]. This bonding is the key to the stabilized PAN's intrinsic electronic conductivity. The existence of these two Raman shifts is direct proof that this heat treatment regiment is effective in forming cyclic pyridinic segments and conjugated intermolecular crosslinks in the electrode's PAN binder.

Figure 18b presents the XRD spectra of heat-treated Sn-PAN electrodes with various mass loadings of PAN binder. The spectra of an uncoated piece of copper foil current collector and an untreated 100% nSn slurry-coated electrode were included for reference. The current collector's peaks are representative of the FCC crystal structure of pure copper. The spectrum of the untreated 100% nSn slurry-coated electrode shows prominent peaks attributed to the body centered tetragonal crystal structure of metallic β-tin. Small peaks associated with tetragonal tin (II) oxide (SnO) are also present. This confirms the existence of a thin native oxide layer on the surface of the untreated tin nanoparticles. Upon heat treatment, the 100% nSn electrode's tin peaks shrink in magnitude as the peaks representing SnO grow dramatically. This oxidation occurred despite the short heat treatment being conducted under a continuous flow of pure argon purge gas. All attempts to prevent this oxidation with longer pre heat treatment purges were unsuccessful. This suggests that some amount of oxygen was strongly adsorbed or chemisorbed to the electrodes' surface prior to heat treatment and could not be easily removed [62]. Reports have shown that SnO can self catalytically grow on tin nanostructures upon heat treatment to ~270°C in inert gas environments containing < 0.01% oxygen [63,64]. This suggests that it may be difficult to prevent the oxidation of any uncoated tin during the PAN cyclization process as the exposed nanoparticles are extremely reactive due to their high surface energies. Fortunately,

SnO is still capable of electrochemically alloying with lithium [65]. The spectra of the heat-treated Sn-PAN electrodes display a clear trend of increasing β-tin peak magnitude and decreasing SnO peak magnitude with increasing PAN content. This shows that the oxidation of the tin nanoparticles upon heat treatment can be effectively mitigated by complete encapsulation in PAN binder.

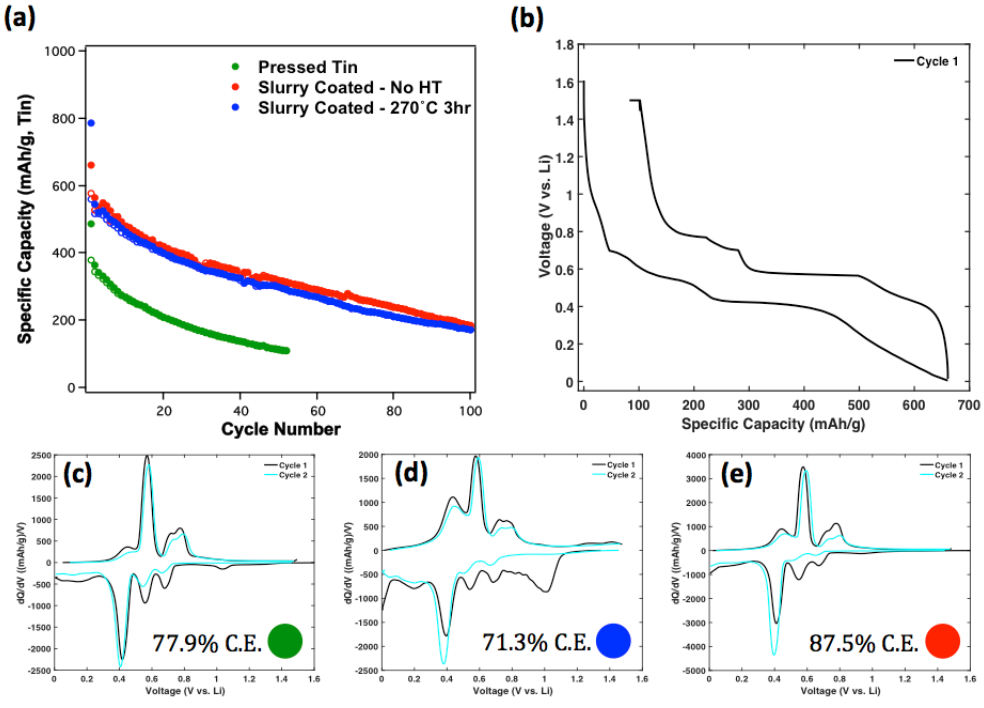

Figure 19. (a) Cycling Data (b) First Cycle Voltage Profile (Red Cycling Data) and (c-e) dQ/dV Spectra for Three 100% nSn All-Solid-State Electrodes

Figure 19a shows the cycling data of three 100% nSn electrodes, each containing ~2 mg of active tin nanoparticles. The data in green represents the cycling performance of an electrode prepared by hand spreading tin nanoparticles over a prepressed SSE separator before final compaction, while the data in red and blue represents two sheet-style electrodes prepared by evenly blading a suspension of tin nanoparticles over a copper current collector and drying. While all three electrodes were capable of cycling without any conductive additives, the difference in capacity between the two styles is clear. This shows that a uniformly dispersed slurry-coated electrode enables a higher degree of active material utilization than the more traditional bulk style pressed powder all-solid-state electrode where active primary particles tend to be agglomerated and isolated.

The two slurry-coated electrodes, which were punched from the same electrode sheet, differ in that one was heat-treated before cycling (blue) while the other was not (red). The first cycle voltage profile of the untreated electrode is presented in Figure 19b. This can be referenced as a great example of the distinct plateaus representing the various crystallographic phases of lithiated tin, Li_xSn. The first and second cycle dQ/dV spectra of the three 100% nSn electrodes are presented in Figures 19c-e. The two slurry-coated electrodes achieve significantly different first cycle specific lithiation capacities, 660 mAh/g for the untreated electrode and 786 mAh/g for the heat-treated electrode. Their delithiation capacities are nearly identical. This can be attributed to the large amount of SnO present in the heat-treated electrode (Figure 18b). Upon initial lithiation, an irreversible reaction occurs between the oxygen in SnO and lithium resulting in the formation of lithium oxide (Li_2O) and pure tin. This irreversible capacity is clearly identified by a broad lithiation peak around 1.1 V that disappears on subsequent cycles. Once the Li_2O is formed, it remains as an inactive amorphous matrix while the tin is allowed to reversibly alloy with lithium [65]. This trapping of lithium in amorphous Li_2O accounts for the poor first cycle coulombic efficiency (CE) of the heat-treated electrode (71.3%) compared to the untreated electrode (87.4%). The similarity of the two electrodes' first cycle delithiation capacities indicates that practically all of the electrochemically active tin was reclaimed from the oxide after its initial lithiation. The near identical performance (Figure 19a) of the two slurry-coated electrodes further supports this point and suggests that the presence or amount of SnO has little impact on the long-term cycling of the heat-treated Sn-PAN electrodes in this study.

Figures 20a-b display the cycling performance of six slurry-coated Sn-PAN electrodes with various mass loadings of PAN. Their first cycle coulombic efficiencies are plotted in Figure 20c. This data shows that the optimum mass loading of PAN binder is approximately 5 wt. %. The 5% PAN electrode achieved the largest first cycle specific lithiation capacity of any electrode tested; 945.7 mAh/g when normalized to total mass of tin active materials and 898.4 mAh/g when normalized to total electrode mass. This electrode was then able to maintain an electrode specific capacity of more than 643 mAh/g after 100 cycles at a 0.1C rate, corresponding to 87% retention of its second cycle's capacity. Furthermore, this 5% PAN electrode displayed the largest first cycle coulombic efficiency (>85%) of any cell tested. Its CE then averaged ~99% for the remainder of its cycles at 0.1C. This is an important metric to consider when transitioning to a full-cell configuration where lithium content is limited. The 5% PAN electrode displayed a far greater 1st cycle capacity compared to the 100% nSn electrodes (Figure 19a), nearly achieving the theoretical limit for tin (959 mAh/g). This highlights the ability of PAN to connect and utilize all of the electrode's active materials. To our knowledge, this is the highest capacity sheet-style electrode ever reported in an all-solid-state battery, and its performance surpasses that of similar nSn-based slurry-coated electrodes cycled in conventional coin cells [66].

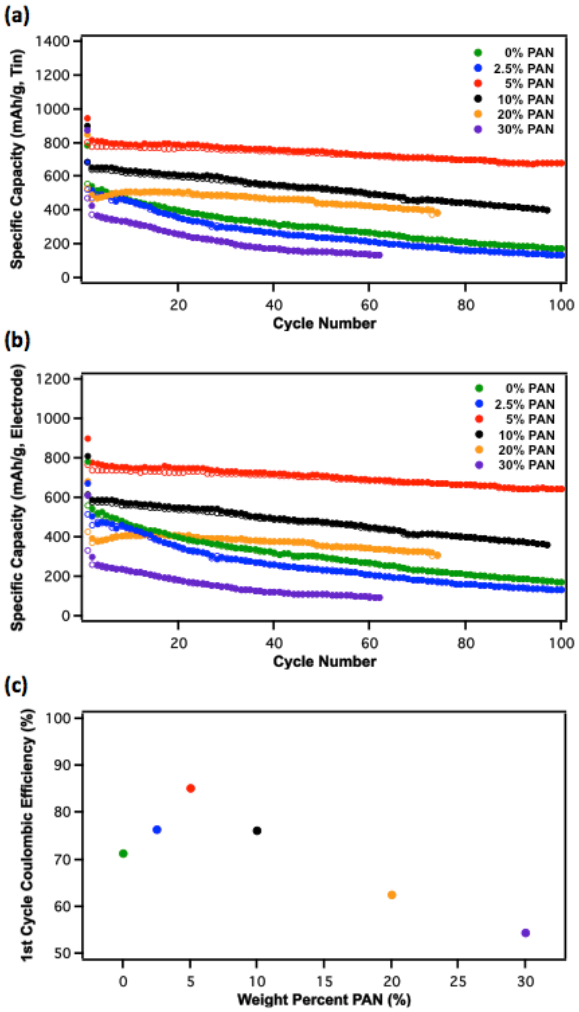

Figure 20. Cycling Performance of Heat-Treated Sheet-Style Sn-PAN Electrodes with Capacities Normalized to Mass of (a) Active nSn Particles and (b) Total Mass of Electrode with (c) First Cycle Coulombic Efficiencies of the All-Solid-State Half Cells

A high resolution SEM image showing the surface morphology of one of these heat-treated 5% PAN electrodes is presented in Figure 21a. The tin nanoparticles are evenly dispersed with some larger porosity still visible. Figure 21b provides a higher magnification view of the same electrode's surface. This image gives a clear view of the electrode's spherical tin nanoparticles, which range in diameter from ~50-200 nm. At this magnification, the PAN binder can be seen bridging gaps between neighboring tin nanoparticles. This mixed conducting PAN matrix helps to bind the active tin nanoparticles together. It also acts to electrochemically link them to the current collector, preventing their irreversible isolation with cycling.

The internal microstructure a heat-treated 5% PAN electrode is shown in Figure 21c. Pores can be seen throughout the electrode's approximately 7 μm thick Sn-PAN layer. The concentration of PAN binder appears to be more heavily distributed between the small particles that settled near the electrode's surface. Larger, unfilled pores are present near the interface between the Sn-PAN composite and the Cu-foil. These pores are attributed to the extreme surface roughness of the chemically etched current collector. In the future, the implementation of a calendaring step prior to heat treatment or the use of a polished current collector could improve the interfacial contact between the Sn-PAN and Cu-foil layers.

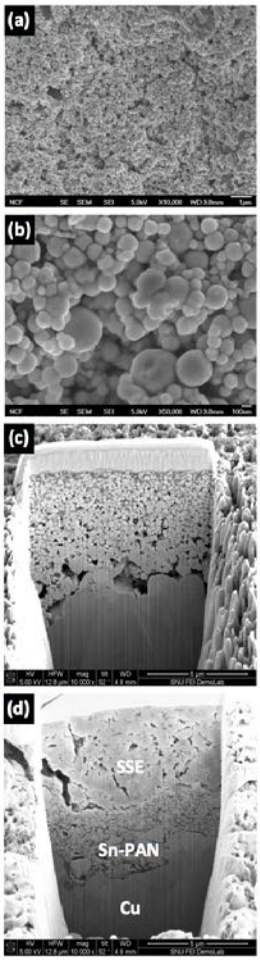

Figure 21. 10,000x (a) and 50,000x (b) High-Resolution SEM Images of the Surface of a Heat-Treated 5% PAN Slurry Coated Electrode and FIB Cross-Section View of a Heat-Treated 5% PAN Slurry Coated Electrode Before (c) and After (d) Assembly of an All-Solid-State Cell

A cross-sectional SEM image of a 5% PAN all-solid-state half-cell is presented in Figure 21d. This ASSC was disassembled for FIB milling without being cycled, so its slurry-coated Sn-PAN electrode remains pristine. A large degree of porosity and cracking can be seen in the thick SSE layer. This is mostly attributed to the stresses involved in the disassembly of the ASSB and its preparation for FIB milling. The thickness of the Sn-PAN layer was halved upon assembly of the cell, leading to a reduction in its observable porosity. This compaction resulted in conformal interfacing between the Sn-PAN composite and both the Cu-foil current collector and SSE separator. The densification of the electrode also enabled it to achieve outstanding 1st and 100th cycle volumetric lithiation capacities of 3404.3 Ah/L and 2438.6 Ah/L based on its observed pristine thickness.

A simple model is proposed to approximately calculate the PAN coating thickness in the slurry-coated Sn-PAN electrodes. The model, shown in Figure 22, is composed of a single tin particle with radius r encased in a dense shell of PAN with thickness t. This model relies on the assumptions that the tin nanoparticles are perfectly spherical and that the binder conformally encapsulates them evenly while neglecting any interparticle connectivity.

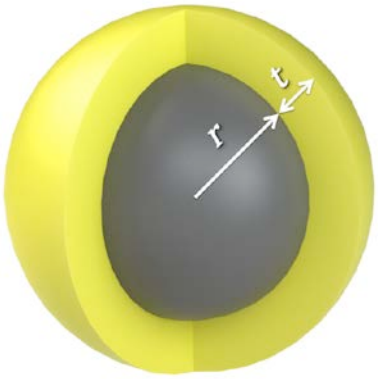

Figure 22. Model Tin Particle used for Spherical Core-Shell Calculations to Estimate PAN Coating Thickness

Taking the average tin nanoparticle diameter to be 120 nm (Figure 21b), the approximate binder coating thickness in the optimal 5% PAN electrode is ~5.9 nm. Piper et al. found the same binder thickness to be optimal in their study of the Si-PAN system [31]. This thickness is also very close to what Xun et al. found to perform the best when they cycled the same tin nanoparticles in an alternative electronically conductive binder [66].

Reducing the PAN content below 5% had a negative impact on the slurry-coated electrode. Figures 20a-b show that the 2.5% PAN electrode displayed a cycling performance practically equivalent to the solution-coated electrode prepared with no binder. The approximate PAN coating thickness calculated for this electrode is only 3 nm. This suggests that while 5% PAN is enough to conformally encapsulate the majority of the tin nanoparticles in a tough, mixed conducing matrix, the 3 nm thick coating in the 2.5% PAN electrode is not effective at holding the electrochemically active particles together and preventing their delamination from the copper current collector with cycling. The only significant differences in the performance of the 0% and 2.5% PAN electrodes are their first cycle capacities and coulombic efficiencies, which indicates that this amount of binder did little more than prevent some of the active tin particles from oxidizing during the cyclization process. This is further emphasized in the XRD data (Figure 18b).

Increasing the electrodes' PAN content beyond 5% resulted in reduced capacity and first cycle coulombic efficiency. The electrode specific capacity decreases as the mass loading of inactive binder in the electrodes grows. Furthermore, some tin particles may become so deeply imbedded in the binder that they are effectively electrochemically isolated at a 0.1C cycling rate and unable to contribute to the electrode's capacity. As the mass loading of binder increases to 10-30%, the approximate PAN coating thickness grows from 11.4 nm to 32.3 nm, respectively. With this increase in PAN, the morphology of the electrode changes from tin particles linked together by a thin coating of PAN to tin particles dispersed throughout a dense matrix of PAN (see Figure 17). Although the PAN binder displays mixed conductivity, increasingly thick coatings will increase resistance in the electrode. These thick, dense regions of PAN are also likely to be more brittle than the conformal thin film coatings present in the 5% PAN electrode. This would make the PAN-rich electrodes more prone to pulverization under the volumetric expansion of the tin nanoparticles, which could explain the steady trend of decreasing 1^{st} cycle coulombic efficiency with increasing PAN content beyond 5 wt. %.

Figures 23a-b display the 1^{st} and 50^{th} cycle dQ/dV plots for the Sn-PAN electrodes shown in Figures 21a-c. The first cycle spectra of the electrodes containing 2.5 - 10% PAN look relatively similar. They all contain the peaks associated with the lithiation/delithiation of tin with no observable overpotentials (see Figure 19). This suggests that the thin coatings of mixed conducting PAN binder present no real barrier to lithiation in these electrodes. The broad lithiation peak attributed to the irreversible conversion of SnO to Li_2O (~1 V) is faintly present in the 2.5% PAN electrode's first cycle spectrum, but the magnitude of this peak greatly diminishes as the PAN content of the electrodes increases. This agrees with our analysis of the XRD data in Figure 18b. The characteristic tin peaks are no longer distinguishable in the 20% and 30% PAN electrodes' first cycle spectra. Instead, a single large lithiation peak is observed around 0.18 V. This change in the dQ/dV spectra can be attributed to the development of a large overpotential in the electrodes. Due to its low density relative to tin, PAN mass loadings of 20 - 30 wt.% correspond to volume fractions of binder in the electrode reaching 60 - 72.5%. This means that on average, neighboring tin nanoparticles are separated by approximately 21.9 - 32.3 nm of inactive PAN. The sluggish diffusion of Li-ions and electrons through these thick layers of cyclized PAN clearly shifted the electrodes' reaction potentials to lower than equilibrium voltages. This means that the initial application of a discharging current resulted in significant polarization of the 20% and 30% PAN electrodes. It is interesting that while the first cycle lithiation peaks of the 20% and 30% PAN electrodes greatly differ from the other electrodes' dQ/dV spectra, their delithiation peaks show little to no overpotential in comparison. This suggests that a change may have occurred in the PAN binder upon its initial lithiation. This change could be related to the diffusion of mobile Li-ions through the mixed conducting binder leading to an equalized concentration gradient in the polymer and reduced resistance upon delithiation. It could also be the result of electrode pulverization isolating all but the most easily reached tin particles. Unfortunately, the exact reason for this interesting phenomenon is currently unknown.

The 50th cycle dQ/dV spectra of the same six cells are plotted in Figure 23b. The disappearance of peaks from the 2.5% PAN electrode is consistent with its irreversible capacity loss due to insufficient binder adhesion. Both the lithiation and delithiation peaks of the 5% and 10% PAN electrodes remained relatively constant in size but have begun to blend together with cycling. This can be attributed to the gradual amorphousization of the active materials [66]. It is interesting that the lithiation overpotential observed in the 20% and 30% PAN electrodes has disappeared with cycling. This could be the result of the unknown phenomenon alluded to above.

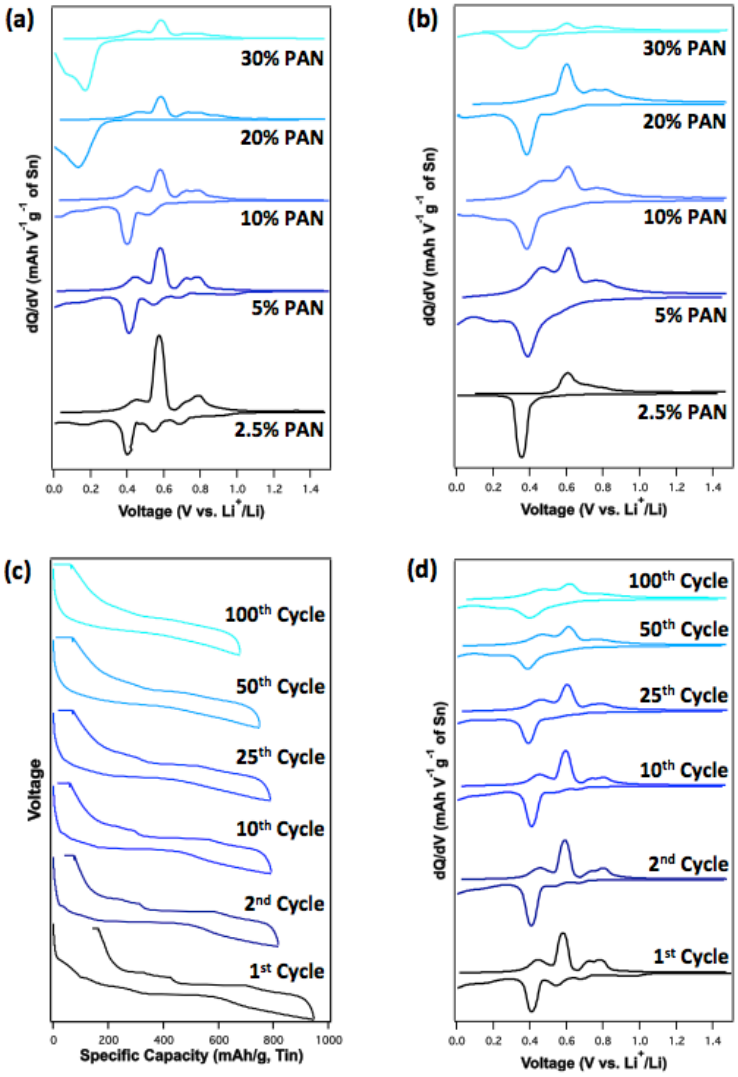

Figure 23. 1st (a) and 50th (b) Cycle dQ/dV Spectra of the Heat-Treated Sheet Style Sn-PAN Electrodes with Select Voltage Profiles (c) and dQ/dV Spectra (d) of a 5% PAN Sheet Style Electrode

Figures 23a-b depict the dQ/dV spectra and voltage profiles of the 5% PAN electrode over various cycles. While the individual plateaus and peaks are initially very distinct in the early cycles, the plots begin to become more sloped and indistinct with cycling. This can be attributed

to the gradual loss of crystallinity of the tin active materials [66]. The consistency of the plots over 100 cycles speaks to the PAN binder's ability to hold the electrode together and prevent the electrochemical isolation of active tin particles. No overpotential develops in the electrode with cycling showing that the PAN binder was able to quickly move Li-ions and electrons through the electrode while accommodating the tin particles' volume changes without pulverizing.

We conducted a rate study on the 5% PAN electrode to investigate its transport properties in an all-solid-state Li-ion half-cell (Figure 24). At a rate of 5C, the electrode maintained an outstanding specific capacity of 216 mAh/g. Achieving a capacity that large at a 5C rate further proves that the cyclized PAN provides facile ionic and electronic transport in the cell. The excellent rate capability of this electrode in an all-solid-state cell also alludes to its ability to intimately interface with the SSE separator, allowing for adequate ion transport and capacity retention at large current densities.

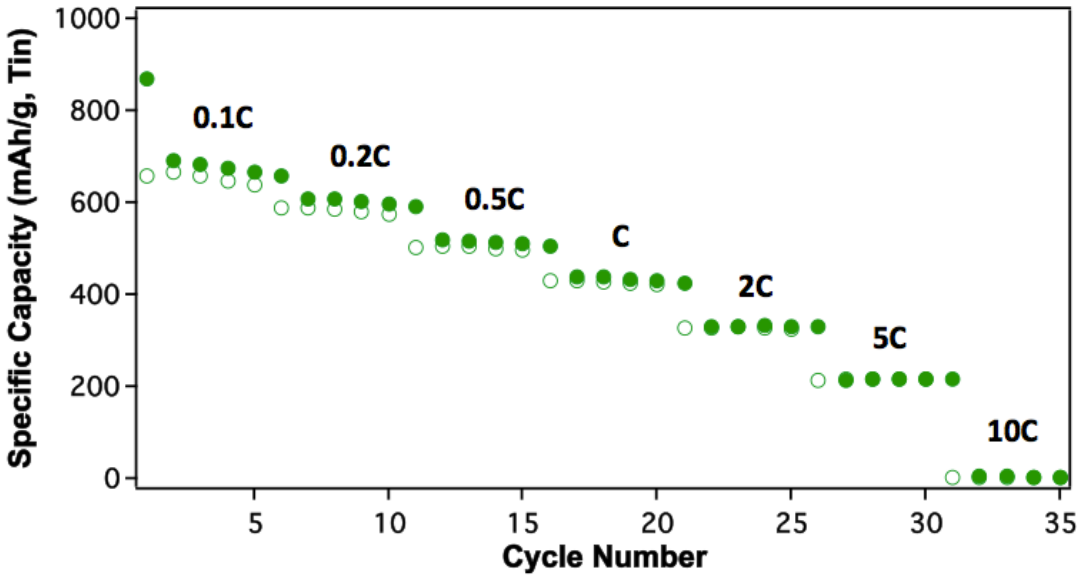

Figure 24. Rate Capability of a 5% PAN Electrode Cycled in an All-Solid-State Half Cell

To increase the capacity of our sheet style Sn-PAN electrode, we decided to introduce nano-silicon active materials through a multi-layered slurry coated approach. In a previous report [57], we showed that a composite electrode prepared by mixing tin, silicon and solid electrolyte particles was capable of achieving a large, relatively stable capacity of around 700 mAh/g. Analysis of the electrode showed that both tin and silicon contributed to the cells overall capacity. As silicon is known for its poor reversibility due to pulverization and isolation with cycling, the stability of this electrode's capacity was attributed to the Sn lithiating prior to Si, resulting in an insitu conformal confining pressure on the Si nanoparticles restricting their expansion and thus retaining their capacity. Our goal was to take advantage of this insitu confining pressure to enable a slurry coated sheet style Sn-Si hybrid anode through a multi-layer architecture.

Figure 25a shows a cross sectional schematic of our tri-layered electrode. This electrode was bladed onto a copper foil current collector via a three-step process, with drying steps included after the application of each layer. This is, undoubtedly, the first time any such electrode architecture has been investigated for use in an ASSB.

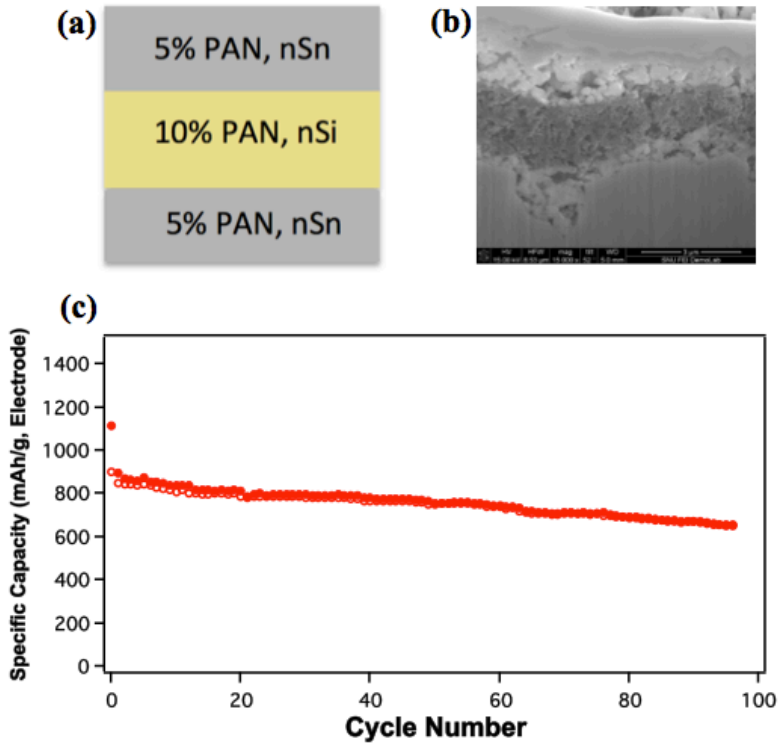

Figure 25. Cross Sectional Schematic (a) and SEM Image (b) of a Pristine Multilayered Sheet Style Electrode and its Cycling Performance (c) in an All-Solid-State Half Cell

A cross-sectional SEM image of a pristine multilayered electrode is presented in Figure 25b. A dark ~2 μm thick nSi-PAN layer can clearly be seen sandwiched between two ~1 μm thick layers of nSn-PAN. The nSn-PAN layer fills the textured surface of the chemically etched copper foil current collector (bottom layer of cross-sectional image) quite well. Some porosity can be seen in the electrode, especially in the tin layers where the relatively large particles have an average diameter >100 nm. Upon pressing, this porosity is expected to diminish as the more ductile tin particles deform to more conformally interface with the nSi-PAN, copper foil and SSE layers.

Figure 25c displays the cycling performance of this multi-layered electrode in an ASSB. This electrode had a total mass of 3.49 mg (excluding the mass of the copper current collector) and was cycled in a voltage window of 5 mV-1.5 V (vs. Li^+/Li). The tri-layered electrode achieved a first cycle electrode specific capacity of 1115 mAh/g corresponding to an outstanding areal capacity of 3.44 mAh/cm^2. Over 80% of this initial lithiation capacity was reversible, and after 97 charge-discharge cycles, 73% of its second cycle lithiation capacity was maintained. These results show that our goal of pairing the capacity of Si-PAN and the stability of Sn-PAN was largely achieved with this multi-layered electrode.

To better understand the capacity retention of the tri-layered electrode, two bi-layered slurry coated electrodes were prepared and cycled. The cycling performance of these two bi-layered electrodes is compared to the performance of the tri-layered electrode along with a single layered Si-PAN electrode in Figure 26a. This plot shows that the outstanding stability of the tri-layered electrode is dependent on the combination of all three layers, and that the removal of one layer compromises the performance of the electrode. Before this test, we hypothesized that the tri-layered electrode benefited from the ductility of its tin layers. This data appears to confirm this hypothesis. Although the pure Si-PAN electrode (Figure 18b) displays the largest electrode specific capacity, it suffers from constant capacity loss with cycling. As mentioned previously in this report, this irreversible capacity loss can be attributed to the pulverization of the electrode. This pulverization, the result of the extreme volumetric expansion/contraction of its silicon active particles, leads to active material isolation and irreversible capacity loss as the Si-PAN composite separates from both the copper current collector and SSE separator. By sandwiching the silicon particles between two layers of tin (Figure 18c) this delamination and isolation is largely prevented, resulting in the outstanding cycling performance of the tri-layered electrode. These soft layers act as a buffer to silicon's extreme volume changes with cycling. Furthermore, as tin lithiates prior to silicon, its volumetric expansion can actively compress and confine the silicon particles. This insitu compressive stress may restrict the volumetric expansion of the sandwiched silicon particles upon lithiation, resulting in less pulverization and therefore increased cycling performance. It will also help to ensure that the silicon particles always remain electrochemically connected within the tri-layered pellet.

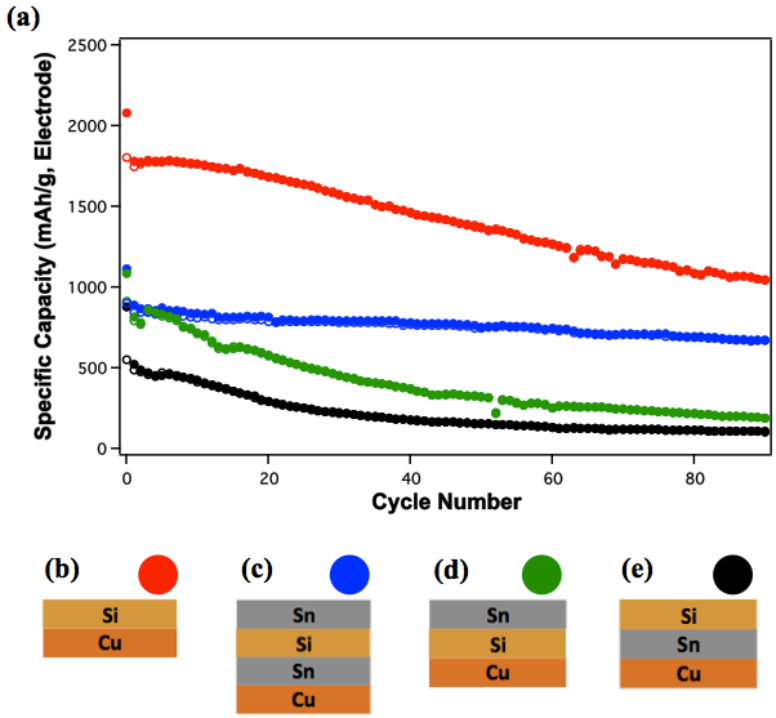

Figure 26. Cycling Performance (a) of Various Multilayered All-Solid-State Sheet Style Electrodes and their Corresponding Cross Sectional Schematics (b-e)

The cycling stability of the bi-layered electrodes further demonstrates the importance of the tri-layered design. The first bi-layered electrode (Figure 26d), which we will now refer to as B1, achieves a large initial electrode specific capacity. This large first cycle lithiation capacity nearly matches that of the tri-layered electrode, suggesting that both of the B1 electrode's active layers were largely utilized. The B1 electrode's capacity rapidly decays in the subsequent cycles. We propose that the electrode's poor performance can be attributed to the interface between the copper current collector and the Si-PAN composite layer. As the electrode cycles, we imagine that the Si-PAN electrode's large volumetric expansion/contraction will lead to its gradual delamination from the copper current collector despite the strong adhesion of the PAN binder. As this Si-PAN layer breaks away from the current collector, active particles will become electrochemically isolated resulting in an irreversible capacity loss. This problem is prevented in the tri-layered electrode as the relatively ductile Sn-PAN layers accommodate the expansion of the brittle silicon particles while exerting an insitu compressive stress from both sides. In the absence of a Sn-PAN buffer, the Si-PAN layer pulverizes against and pulls away from the hard copper current collector upon lithiation and delithiation, respectively.

Electrode B2 (Figure 26e) shows a similar trend of irreversible capacity loss with cycling. This suggests that the interface between the electrode and the SSE separator is also quite fragile. Because the Sn-PAN and tri-layered electrodes presented earlier display more stable capacities with prolonged cycling, we postulate that the B2 electrode's rigid Si-PAN layer leads to a large degree of delamination from the SSE separator. One interesting difference between the B2 and B1 electrodes is their electrode specific capacities. Because the slurry deposition procedure was kept constant between the two electrodes, it should be safe to assume that the mass ratio of silicon to tin should be similar in B1 and B2. With that said, both cells should achieve relatively identical electrode specific capacities. The fact that the two electrodes' capacities do vary suggests that their two layers are not utilized to the same extent. This hypothesis will be discussed in further below.

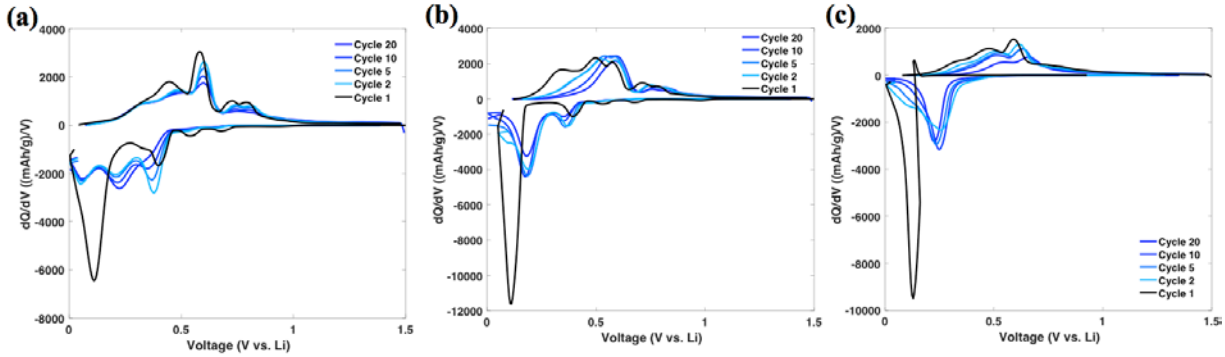

Figure 27. dQ/dV Spectra of the Tri-Layered (a) and Bi-Layered Electrodes B1 (b) and B2 (c)

Select dQ/dV spectra for the tri-layered, B1 and B2 electrodes are presented in Figures 27a-27c, respectively. These plots will help to give insight into the source of the electrodes' capacities throughout cycling. Focusing first on the tri-layered electrode's spectra (Figure 27a), four main peaks can be observed in its initial lithiation curve. The first three peaks, centered at the potentials 0.69 V, 0.54 V and 0.4 V, can all be attributed to the lithiation of the electrode's tin layers. The expansion of these tin layers will undoubtedly exert a compressive stress on the middle silicon layer, improving its interfacial contact with both tin layers before it lithiates at a lower potential. The large peak centered ~0.12 V is representative of the two-phase transition of crystalline silicon to lithiated amorphous silicon. In our previous reports on Si-based mixed

composite electrodes, we found that this peak appeared nearer to 0.17V vs. Li^+/Li [57]. Assuming this to be closer to the equilibrium voltage for this reaction, the shift in reaction potential observed in Figure 27a can be attributed to an overpotential. This overpotential, or barrier to reaction, is the result of the confinement of the silicon particles by the tough cPAN binder and the compressive stress exerted by the neighboring Sn-PAN layers.

Upon delithiation, five distinct peaks can be observed in Figure 27a. The first peak, centered around 0.33 V, represents the delithiation of the highly lithiated amorphous silicon phases. The second peak, centered around 0.44 V, is more difficult to identify. It can be partially attributed to the delithiation of tin, but also contains contribution from the peaks representing the delithiation of amorphous silicon (~0.48V) and the two-phase delithiation of the highly lithiated crystalline silicon phase, $Li_{15}Si_4$. The large sharp peak ~0.58 V is characteristic of tin, as are the two twin peaks centered at 0.71 V and 0.79 V.

With continued cycling, it is clear that the primary lithiation peak associated with tin (~0.4V) rapidly decreases with cycling while those associated with the lithiation of various amorphous Li_xSi phases (~0.21V & ~0.05V) remain relatively constant. A similar trend is apparent in the delithiation peaks above. A more thorough discussion of the capacity contributions of silicon and tin in the tri-layered electrode will be presented below.

Figure 27b depicts select dQ/dV spectra of the bi-layered electrode, B1. The first cycle profile shows the distinct peaks of both tin and silicon. The lithiation profiles differ from those in Figure 27a in that only one large silicon lithiation peak (~0.25V) remains visible throughout cycling. This peak, which represents the formation of lower lithiated amorphous Li_xSi phases, displays a large overpotential in comparison to the tri-layered electrode. This can be attributed to the previously postulated delamination of the Si-PAN layer from the current collector. The large increase in resistance caused by this rapid degradation of the electrode, specifically the barrier for charge transfer at the now compromised electrode / current collector interface, would lead to the development of such an overpotential. This overpotential would then shift the full lithiation potential of the active silicon particles outside of the cell's applied voltage window. The delithiation curves confirm the electrochemical utilization of tin thorough cycling. They also mirror the development of an overpotential in the silicon peaks, which slowly shrink with cycling.

Figure 27c shows the dQ/dV spectra of the bi-layered electrode, B2. These spectra differ from the previous two electrodes' in that the initial lithiation curve shows no peaks that can be clearly attributed to tin. At first glance, this spectrum suggests that the silicon layer effectively blocks the Sn-PAN layer from lithiating, as silicon's initial two-phase reaction with lithium occurs at a potential significantly lower than the lithiation of tin. Upon closer inspection, this cannot be completely true as small tin delithiation peaks (~0.58 V) consistently appear on the topside of the plot throughout cycling. This shows that the Sn-PAN layer, which separates the Si-PAN composite from the copper current collector, is utilized to some degree. Despite the consistent presence of tin related delithiation peaks, no peaks representing the lithiation of tin are ever observed. This shows that the Si-PAN layer impedes the lithiation of the Sn-PAN layer, meaning the Sn-PAN layer cannot alloy with lithium until voltages much lower than its equilibrium reaction potential. In other words, the Si-PAN layer must fully begin its reaction with lithium before any Li-ions are allowed to diffuse into the Sn-PAN layer hidden below. Because of this, the peak representing the lithiation of the Sn-PAN layer is combined with the peak commonly thought to represent the lithiation of amorphous silicon. This single lithiation peak shows a smaller overpotential than was observed in spectra in Figure 27b. This suggests

that the soft tin buffer layer separating the copper current collector from the high capacity Si-PAN composite is critical to maintaining conduction pathways through the electrode. This data is also proof that the bottom most Sn-PAN layer contributes to the overall capacity of the tri-layered electrode and is not simply there to improve interfacial coupling with the copper current collector.

To further progress the performance of our slurry coated all-solid-state sheet style electrodes, it was decided to abandon tin as an active material and focus on a full Si-PAN system. Silicon achieves a specific capacity nearly four times greater than tin and does so at a lower average operating potential. Furthermore, the cyclization process requires heat treatment temperatures exceeding the melting point of tin. This leads to undesirable variability in the electrodes' microstructure. It can also result in the growth of thick oxide layers on the surface of the tin particles, which greatly increases the irreversibility of the cell's initial lithiation capacity. This is seen as a major issue when transitioning to a full cell configuration where the lithium content in the cell must be carefully calculated and budgeted.

In the past, we have had great success cycling Si-PAN anodes in conventional cells utilizing both carbonate and ionic liquid electrolytes [31,34]. These cells displayed large capacities but struggled with stability due to the cyclic growth and exfoliation of parasitic solid electrolyte interphase layers. Our recent discovery that thin coatings of cPAN binder display relatively facile mixed conduction has allowed us to begin to optimize the first ever sheet style silicon anode in an all-solid-state. While we are just beginning to optimize this system, the Si-PAN electrode appears to excel in the solid state environment, surpassing the cycling performances reported in our previous publications.

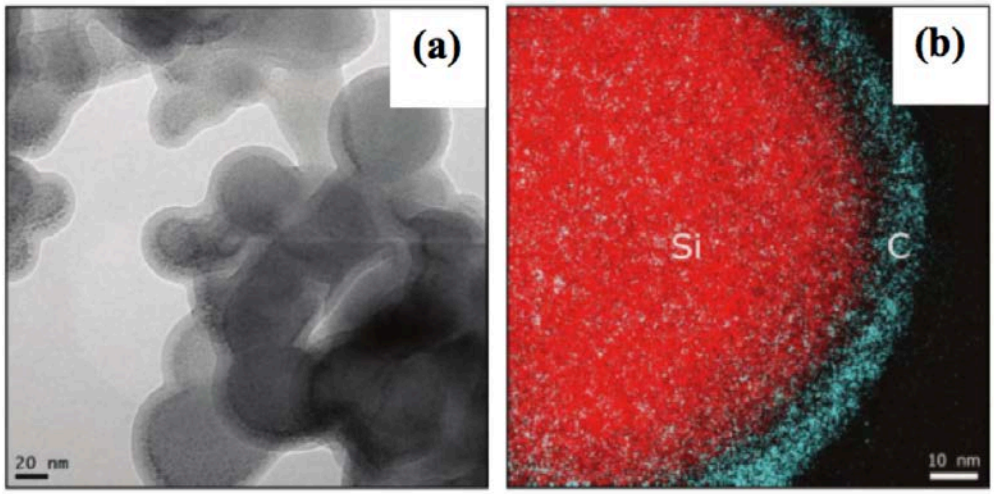

Figure 28. (a) TEM Micrograph of a Pristine Si-cPAN Electrode with (b) EELS Mapping Confirming the Thickness of the Binder Layer

A transmission electron microscope (TEM) micrograph of a pristine Si-cPAN electrode is presented in Figure 28a. This high-resolution image clearly shows ~20-50 nm silicon particles conformally encapsulated and intimately linked by a thin coating of cyclized PAN binder. This binder layer, which is accentuated in the electron energy loss spectroscopy (EELS) elemental

map in Figure 28b, is approximately 10 nm thick. This is thick enough to contain the volumetric expansion of the Si-particles upon lithiation but thin enough to allow the quick passage of both Li-ions and electrons. These images, which were collected for use in one of our previous publications [31], should be representative of the microstructure of the electrodes used in this report as the same slurry composition and preparation procedure was used in both cases.

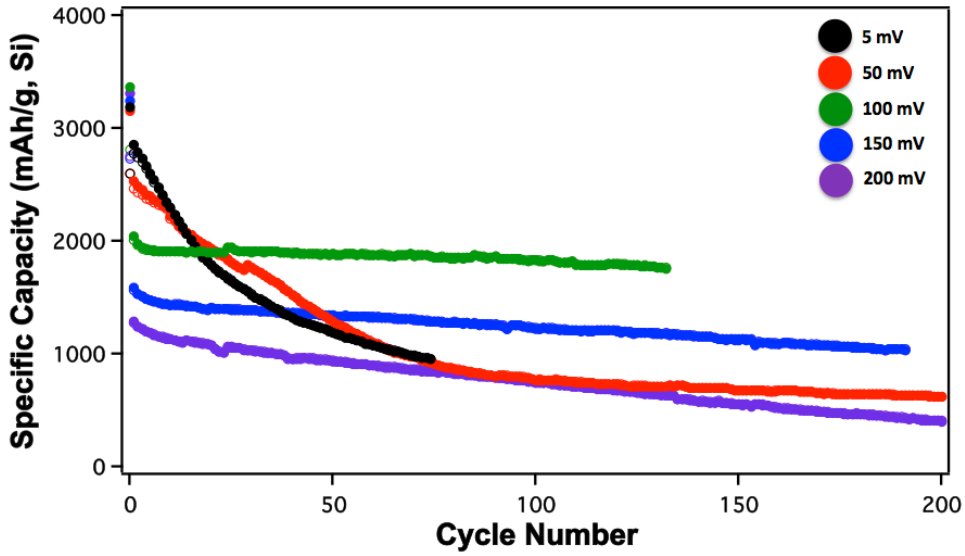

Figure 29. Cycling Performance of Si-cPAN Electrodes with Various Lower Working Potentials

The cycling performance of the 30% PAN slurry coated sheet style silicon anode is presented in Figure 29. Five identical anodes, all containing ~0.9 mg/cm^2 of silicon nanoparticles, were cycled in all-solid-state half cells with an InLi counter electrode. The operating voltage window (*x* V - 1 V vs. Li^+/Li) of the five cells was adjusted so that the effect of the lower potential (*x*) on the cells' capacity and cycling stability could be investigated.

All five cells in Figure 29 underwent an initial conditioning cycling in which they were lithiated, at a C/20 rate, down to 50 mV in order to complete the two-phase transition from pristine crystalline silicon to a lithiated amorphous Li_xSi phase. Upon delithiation back to 1 V (vs. Li^+/Li), the silicon active particles' structure remains amorphous such that all following cycles proceed in a gradual single phase transition between various Li_xSi compositions.

Each of the cells shown in Figure 29 achieves a large first cycle specific lithiation capacity approaching the theoretical limit of silicon (3579 mAh/g for $Li_{15}Si_4$). This suggests that the conformal cPAN matrix was effective in electrochemically linking all of the silicon particles within the sheet style electrode and that the active materials were nearly fully utilized, totally converting their pristine crystalline structure into a disordered amorphous state.

After completion of their initial conditioning step, the cells were left to cycle under their assigned voltage window (*x* V - 1 V vs. Li^+/Li) at a C/10 rate. The resulting cycling data shows two clear trends. The first trend is increasing capacity with decreasing lower voltage limit. The cell with a 5 mV lower limit achieved a second cycle specific lithiation capacity of 2856 mAh/g when normalized to mass of silicon in the anode. On the other hand, the cell limited to 200 mV

achieved a second cycle silicon specific lithiation capacity of only 1291 mAh/g. This large increase in capacity with reduced lower voltage limit comes at the price of extreme volumetric expansion of the active silicon particles. While this large swelling of silicon has been widely accepted to result in active particle pulverization and capacity loss with cycling, the drastic difference between the stability of the cell lithiated to 50 mV and cells with lower limits ≥100 mV suggests that something more than just volumetric expansion is affecting the capacity retention of these cells.

In order to derive a basic understanding of the structural changes occurring within the different Si-PAN electrodes during cycling, select dQ/dV profiles for each all-solid-state half cell were plotted for comparison in Figure 30. The first cycle profile was excluded from all of the plots in Figure 30 as the sharp peak representing the two-phase transition between pristine crystalline silicon and the amorphous lithiated (Li_xSi) phases is practically identical between all five of the cells and its magnitude distracts from the analysis of the structural changes occurring in the following cycles. The second cycle dQ/dV profile of the cell lithiated to 5 mV is displayed in Figure 30a. This plot highlights the four alternate lower limit voltage cutoffs utilized in this experiment with red dots so that their position in relation to a full lithiation profile can be quickly and easily visualized.

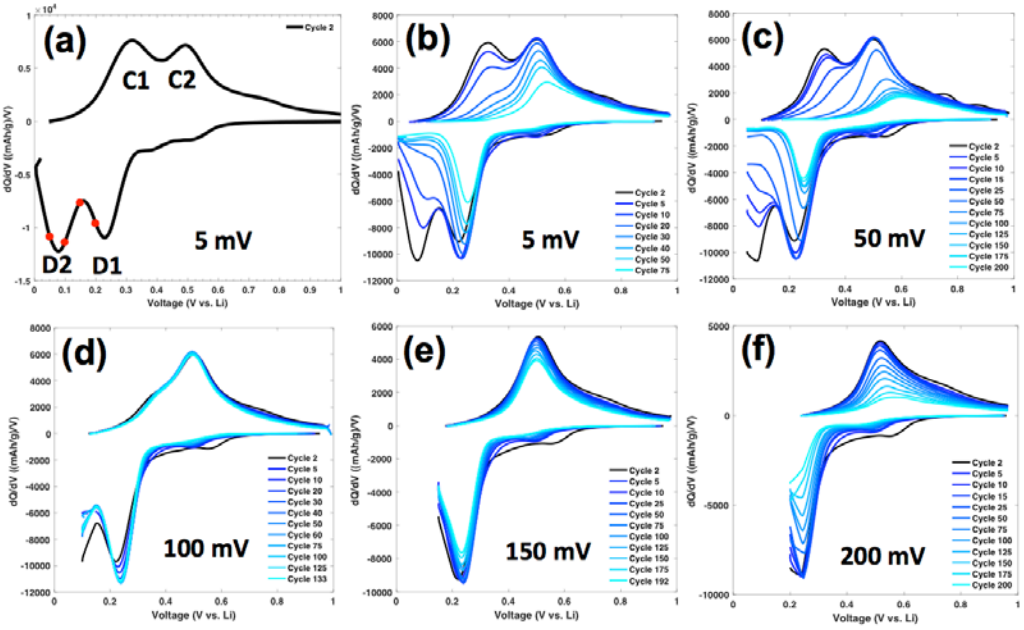

Figure 30. dQ/dV Spectra of Si-cPAN Electrodes Cycled with Various Lower Working Potentials

Two main lithiation or discharge peaks are evident in Figure 30a. The first, which we will call D1, is centered around 0.24 V. This peak represents the formation of lower lithiated amorphous Li_xSi phases. The second peak, D2, centered around 0.8 V represents the formation of more highly lithiated amorphous Li_xSi phases. The delithiation of the fully discharged silicon anode results in two charging peaks, which can clearly be seen on the topside of Figure 30a. These two peaks, centered around 0.3 V and 0.52 V represent the delithiation of the highly and

moderately lithiated Li_xSi phases, respectively. An unidentified lithiation event occurring around 0.55 V is observed in the initial cycles of all of the cells in Figure 30. At this point, we speculate that this peak is related to the decomposition of our binary SSE to form a solid electrolyte interphase layer with either the Si-PAN anode or the InLi counter electrode, but this hypothesis still needs to be experimentally verified in the near future.

Analysis of Figures 30b and 30c shows that much of the initial capacity loss in these deeply discharged electrodes comes about from the rapid reduction of the D2 peak. This failure to form the highly lithiated Li_xSi phases after 10 or more cycles results in the quick disappearance of the C1 charging peak. Limiting the Si-PAN electrode's lower working potential in order to purposefully avoid the formation of the D2 and C1 peaks (Figures 30d and 30e) results in a dramatic increase in the half cell's capacity retention with cycling. Understanding both the macro and microscopic changes involved in the development and transition between the two discharge and charge peaks and the material properties (i.e. conductivity, volumetric expansion, modulus) of their associated amorphous Li_xSi phases may be key to understanding and optimizing the performance of these Si-PAN electrodes. Unfortunately, the current understanding of the structural differences between the various Li_xSi phases during discharging-charging is extremely limited. Furthermore, information about the amorphous Li_xSi bonding environment with prolonged cycling is virtually unknown at this point in time.

Analysis of the dQ/dV plots at hand suggests that the capacity loss is not simply related to electrode pulverization, as no shift or overpotential related to increasing electrode resistance can be observed in any of the plots presented in Figure 30. In fact, the lithiation peaks appear to shift to higher voltages alluding to improved reaction kinetics with cycling. This points to the fact that the Si-PAN system is robust enough to withstand the large volumetric expansion of the silicon particles without fracture or delamination. It also shows that the transport pathways provided by the conformal mixed conducting cPAN binder matrix remain open throughout cycling.

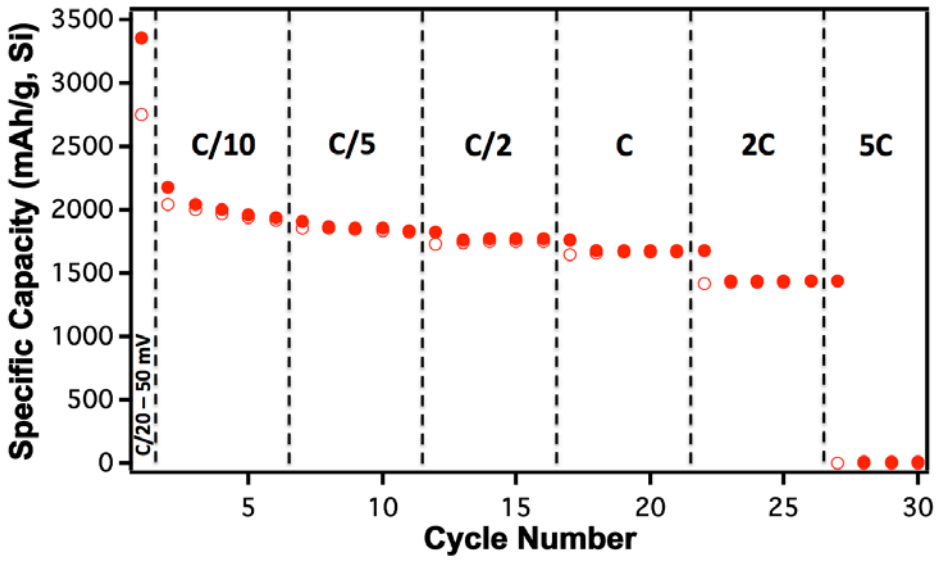

Figure 31. Rate Capability of a Si-cPAN Electrode Cycled in an All-Solid-State Half Cell

This preliminary data provides further evidence of the remarkable mixed conductivity of the commercially available cyclized PAN (cPAN) binder. Silicon is a much poorer conductor than the tin metal nanoparticles we utilized in our previous all-solid-state sheet style electrode. Despite the inherent resistivity of these silicon active materials, our Si-cPAN electrodes still preformed exceedingly well at increased cycling rates. Figure 31 displays the results of an asymmetric rate study performed on one of our Si-cPAN electrodes cycled within an all-solid-state half cell. The voltage window utilized in this experiment was 100 mV - 1 V. This testing was conducted using various charging rates while maintaining a constant C/10 discharging rate. This was done following an initial C/20 conditioning cycle between 50 mV - 1 V. Figure 31 shows very little capacity difference between cycling the Si-cPAN electrode at a C/10 rate compared to a 1C rate. In fact, even at a 2C rate this cell was able to achieve a stable specific lithiation capacity >1300 mAh/g when normalized to mass of silicon. Further increasing the charging current to a 5C rate results in a complete capacity drop which suggests that the maximum cycling rate of the current Si-cPAN system is somewhere around 2C.

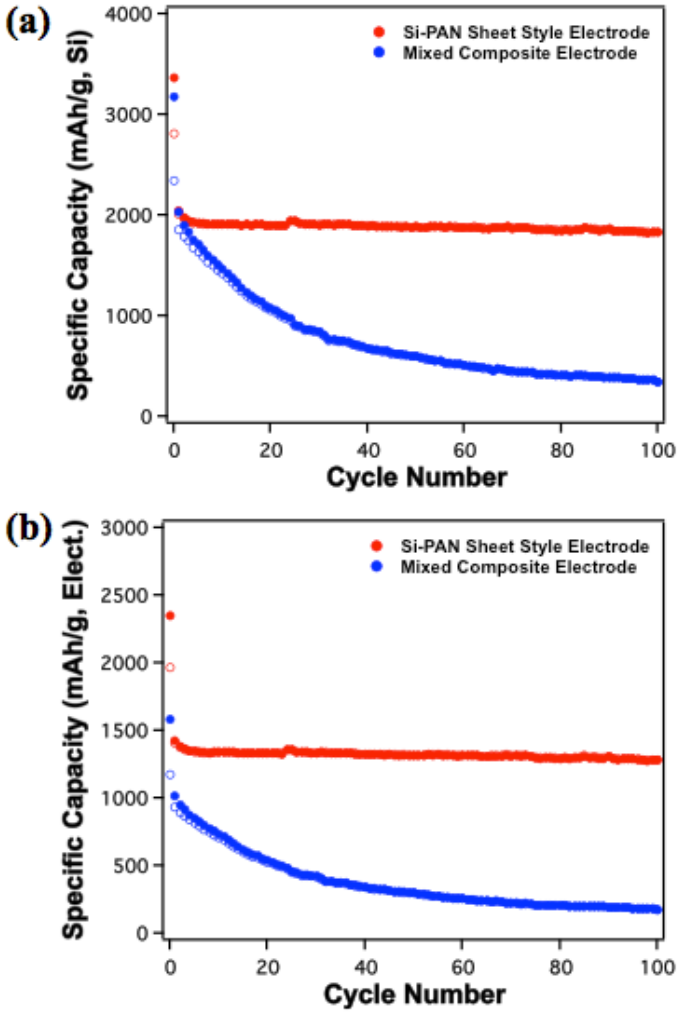

Figure 32. Cycling Performance of a Si-cPAN All-Solid-State Half Cell Compared to Mixed Composite Electrode All-Solid-State Half Cell with Cycling Capacities Normalized to Mass of Silicon (a) or Total Electrode Mass (b)

The best visualization of the outstanding performance of this Si-cPAN system is presented in Figure 32, where the long term cycling stability of one of our sheet style anodes is compared to that of a pressed powder composite electrode (Figure 1b) containing an analogous mass loading of silicon nanoparticles mixed in with carbon conductive additive and SSE powders. When subjected to the same cycling conditions (100 mV - 1 V at a C/10 rate) it is clear that the Si-cPAN system outperforms the mixed composite electrode in practically all metrics. For their first conditioning cycle, the Si-cPAN and mixed composite electrodes achieved similarly high silicon specific lithiation capacities of 3361.5 mAh/g and 3173.5 mAh/g, respectively, but only 73% of the mixed electrode's initial capacity was reversible while the Si-cPAN electrode achieved a first cycle coulombic efficiency >84% (Figure 32a). This difference shows that while the pressed powder composite electrode is capable of fully lithiating most of its silicon particles, the large volumetric expansion and subsequent shrinking of these active materials results in the disruption of the tenuous particle-particle contact points within the electrode culminating in irreversible capacity loss as swollen or fractured silicon nanoparticles are left isolated during the dealloying process. This is much less of an issue in the slurry coated sheet style electrode as the cPAN binder conformally coats, confines and links together the silicon nanoparticles throughout their alloying-dealloying processes.

A nearly identical silicon specific capacity (~2000 mAh/g) is achieved by both cells upon their second cycle lithiation to 100 mV Figure 32a). With that said, a large split is observed when comparing the two cells' electrode specific capacities (Figure 32b), as this takes into account the electrodes' total mass, excluding the weight of the copper foil current collector. Because the mixed composite electrode contains only 50 wt.% active silicon particles, its second cycle electrode specific lithiation capacity is limited to 1014.7 mAh/g. On the other hand, only 30wt.% of the mixed conducting cPAN binder is utilized in the slurry coated sheet style electrode allowing it to achieve a second cycle electrode specific lithiation capacity of 1429 mAh/g.

The Si-cPAN electrode's capacity remained outstandingly stable with cycling. After 100 charge-discharge cycles, this half cell retained 91.2% of its 2^{nd} cycle capacity. The mixed composite electrode only managed to maintain 18.8% of its 2^{nd} cycle capacity.

The poor performance of the mixed composite electrode shows that that style of electrode architecture is simply not effective in practically utilizing a high capacity lithium alloying material such as silicon. This point is further emphasized when evaluating the two cells' coulombic efficiencies. The mixed composite electrode doesn't reach a coulombic efficiency >99% until cycle 40, while the Si-cPAN electrode achieves a coulombic efficiency of 99.2% on just its second cycle at C/5. This shows that the mixed composite matrix is loose and inconsistent, leading to the disruption of interparticle connectivity and active material isolation while the slurry coated sheet style electrode's mixed conducting cPAN binder holds firmly to the silicon nanoparticles despite their swelling and shrinking.

5 CONCLUSIONS

The Si-Ti-Ni (STN) alloy and Stabilized Lithium Metal Powder (SLMP) pre-lithiation technique were developed with conventional liquid Li-ion batteries in mind, but we find that both are also applicable to all-solid-state Li-ion batteries. STN is well suited as an all-solid-state anode active material because the $Li_xTi_4Ni_4Si_7$ matrix of the STN alloy is a mixed conductor. All-solid-state STN composite anodes provide a stable specific capacity of 400 mAh g^{-1} (anode).. To pre-lithiate an all-solid-state Li-ion battery we incorporated SLMP into the STN composite anode powder prior to cell fabrication. This is the first time that the SLMP pre-lithiation technique has been demonstrated in an all-solid-state battery. By pairing the pre-lithiated STN composite anode with a high capacity FeS + S cathode, an all-solid-state Li-ion battery with a specific energy of 225 mWh g^{-1} (cathode + anode) was demonstrated. The results of this study suggest that all-solid-state batteries can achieve acceptable energy densities without the need for a lithium metal anode. By avoiding the use of lithium metal anodes, the engineering challenges associated with the dendritic penetration of cold-compacted glass solid-state electrolyte (SSE) separators can be circumvented.

Next, silicon-carbon composites derived from the industrial waste product coal-tar-pitch were, for the first time, utilized as anode materials in an all-solid-state Li-ion cell. We demonstrated how a simple and industrially scalable solution coating process could be used to encapsulate silicon particles of various shapes and sizes in an amorphous carbon matrix. On its own, this soft carbon material displayed excellent Li-ion capacity and mixed conducting capabilities. Various silicon particle sizes and Si-C:SSE electrode composite ratios were investigated in this report. While it was concluded that the amorphous carbon matrix material was not robust enough to enable the long term utilization of large silicon micro-particles, the optimization of the nano-silicon composite electrode resulted in a half-cell with a 100^{th} cycle specific capacity of 653.5mAh/g (mass electrode) and 1089.2mAh/g (mass Si-C) with a coulombic efficiency >99%.

Lastly, cyclized PAN enabled slurry coated sheet style anodes were developed for use in all-solid-state Li-ion batteries. Cyclized PAN, or cPAN, is well suited as an electrode binder material as it is both mechanically tough and mixed conducting, removing the need for inactive conductive additives that dilute the electrode’s energy density. Through our use of cPAN binder, we are the first to utilize the high capacity Li-alloying materials, silicon and tin, in slurry coated all-solid-state sheet style anodes. Our large mass loadings of these high capacity materials allowed us to achieve outstandingly large and stable cycling capacities. The results of this study suggest that all-solid-state Li-ion batteries can achieve acceptable energy densities without the need for a lithium metal anode. Furthermore, the success of our slurry coated electrode shows that the manufacturing of such a cell may be possible in the very near future.

REFERENCES

[1] Hayashi, A., Ishikawa, Y., Hama, S., Minami, T., and Tatsumisago, M., "Fast Lithium-Ion Conducting Glass-Ceramics in the System Li_2S-SiS_2-P_2S_5," *Electrochemical and Solid-State Letters*, **6**, 3, 2003, pp. A47-A49.

[2] Hayashi, A., Hama, S., Morimoto, H., Tatsumisago, M., and Minami, T., "Preperation of Li_2S-P_2S_5 Amorphous Solid Electrolytes by Mechanical Milling," *Communications of the American Ceramic Society*, **84**, 2, 2001, pp. 477-479.

[3] Tatsumisago, M., Hama, S., Hayashi, A., Morimoto, H., and Minami, T., "New lithium ion conducting glass-ceramics prepared from mechanochemical Li_2S-P_2S_5 glasses," *Solid State Ionics*, **154-155**, 2002, pp. 635-640.

[4] Porz, L., Swamy, T., Sheldon, B.W., Rettenwander, D., Frömling, T., Thaman, H.L., Berendts, S., Uecker, R., Craig Carter, W., and Chiang, Y.M., "Mechanism of Lithium Metal Penetration through Inorganic Solid Electrolytes," *Advanced Energy Materials*, **7**, 20, 2017, pp. 1-12.

[5] Takada, K., Aotani, N., Iwamoto, K., and Kondo, S., "Solid state lithium battery with oxysulfide glass," *Solid State Ionics*, **86-88**, 1996, pp. 877-882.

[6] Kamaya, N., Homma, K., Yamakawa, Y., Hirayama, M., Kanno, R., Yonemura, M., Kamiyama, T., Kato, Y., Hama, S., Kawamoto, K., and Mitsui, A., "A lithium superionic conductor," *Nature Materials*, **10**, 9, 2011, pp. 682-686.

[7] Hashimoto, Y., Machida, N., and Shigematsu, T., "Preparation of $Li_{4.4}Ge_xSi_{1-x}$ alloys by mechanical milling process and their properties as anode materials in all-solid-state lithium batteries," *Solid State Ionics*, **175**, 1-4, 2004, pp. 177-180.

[8] Takada, K., Inada, T., Kajiyama, A., Sasaki, H., Kondo, S., Watanabe, M., Murayama, M., and Kanno, R., "Solid-state lithium battery with graphite anode," *Solid State Ionics*, **158**, 3-4, 2003, pp. 269-274.

[9] Seino, Y., Takada, K., Kim, B.C., Zhang, L., Ohta, N., Wada, H., Osada, M., and Sasaki, T., "Synthesis of phosphorous sulfide solid electrolyte and all-solid-state lithium batteries with graphite electrode," *Solid State Ionics*, **176**, 31-34, 2005, pp. 2389-2393.

[10] Chan, C.K., Peng, H., Liu, G., McIlwrath, K., Zhang, X.F., Huggins, R.A., and Cui, Y., "High-performance lithium battery anodes using silicon nanowires," *Nature Nanotechnology*, **3**, 2008, pp. 31-35.

[11] Ruffo, R., Hong, S.S., Chan, C.K., Huggins, R.A., and Cui, Y., "Impedance Analysis of Silicon Nanowire Lithium Ion Battery Anodes," *The Journal of Physical Chemistry*, **113**, 2009, pp. 11390-11398.

[12] Yao, Y., McDowell, M.T., Ryu, I., Wu, H., Liu, N., Hu, L., Nix, W.D., and Cui, Y., "Interconnected silicon hollow nanospheres for lithium-ion battery anodes with long cycle life," *Nano Letters*, **11**, 7, 2011, pp. 2949-2954.

[13] Goward, G.R., Taylor, N.J., Souza, D.C.S., and Nazar, L.F., "The true crystal structure of $Li_{17}M_4$ (M=Ge, Sn, Pb)-revised from $Li_{22}M_5$," *Journal of Alloys and Compounds*, **329**, 2001, pp. 82-91.

[14] Anani, A., Crouch-Baker, S., and Huggins, R.A., "Kinetic and Thermodynamic Parameters of Several Binary Lithium Alloy Negative Electrode Materials at Ambient Temperature," *Journal of The Electrochemical Society*, **134**, 12, 1987, pp. 3098-3102.

[15] Son, S.B., Kim, S.C., Kang, C.S., Yersak, T.A., Kim, Y.C., Lee, C.G., Moon, S.H., Cho, J.S., Moon, J.T., Oh, K.H., and Lee S.H., "A Highly Reversible Nano-Si Anode Enabled by Mechanical Confinement in an Electrochemically Activated $Li_xTi_4Ni_4Si_7$ Matrix," *Advanced Energy Materials*, **2**, 10, 2012, pp. 1226-1231.

[16] Yersak, T.A., Stoldt, C., and Lee, S.H., "Electrochemical Evolution of an Iron Sulfide and Sulfur Based Cathode for All-Solid-State Li-Ion Batteries," *Journal of The Electrochemical Society*, **160**, 8, 2013, pp. A1009-A1015.

[17] Yersak, T.A., Yan, Y., Stoldt, C., and Lee, S.H., "Ambient Temperature and Pressure Mechanochemical Preparation of Nano-$LiTS_2$," *ECS Electrochemistry Letters*, **1**, 1, 2012, pp. A21-A23.

[18] Jarvis, C.R., Lain, M.J., Gao, Y., and Yakovleva, M., "A lithium ion cell containing a non-lithiated cathode," *Journal of Power Sources*, **146**, 1-2, 2005, pp. 331-334.

[19] Jarvis, C.R., Lain, M.J., Yakovleva, M.V., and Gao, Y., "A prelithiated carbon anode for lithium-ion battery applications," *Journal of Power Sources*, **162**, 2, 2006, pp. 800-802.

[20] Lewis, I.C., "Chemistry of pitch carbonization," *Fuel*, **66**, 11, 1987, pp. 1527-1531.

[21] Wang, Y.X., Chou, S.L., Kim, J.H., Liu, H.K., and Dou, S.X., "Nanocomposites of silicon and carbon derived from coal tar pitch: Cheap anode materials for lithium-ion batteries with long cycle life and enhanced capacity," *Electrochimica Acta*, **93**, 2013, pp. 213-221.

[22] Oh, D.Y., Kim, D.H., Jung, S.H., Han, J.G., Choi, N.S., and Jung, Y.S., "Single-step wet-chemical fabrication of sheet-type electrodes from solid-electrolyte precursors for all-solid-state lithium-ion batteries," *Journal of Materials Chemistry A*, **5**, 39, 2017, pp. 20771-20779.

[23] Sakuda, A., Kuratani, K., Yamamoto, M., Takahashi, M., Takeuchi, T., and Kobayashi, H., "All-Solid-State Battery Electrode Sheets Prepared by a Slurry Coating Process," *Journal of The Electrochemical Society*, **164**, 12, 2017, pp. A2474-A2478.

[24] Yamamoto, M., Terauchi, Y., Sakuda, A., and Takahashi, M., "Binder-free sheet-type all-solid-state batteries with enhanced rate capabilities and high energy densities," *Scientific Reports*, **8**, 1, 2018, pp. 2-11.

[25] Gong, L., Nguyen, M.H.T., and Oh. E.S., "High polar polyacrylonitrile as a potential binder for negative electrodes in lithium ion batteries," *Electrochemistry Communications*, **29**, 2013, pp. 45-47.

[26] Bashir, Z., "A critical review of the stabilisation of polyacrylonitrile," *Carbon*, **29**, 8, 1991, pp. 1081-1090.

[27] Rahaman, M.S.A., Ismail, A.F., and Mustafa, A., "A review of heat treatment on polyacrylonitrile fiber," *Polymer Degradation and Stability*, **92**, 2007, pp. 1421-1432.

[28] Arbab, S., Mirbaha, H., Zeinolebadi, A., and Nourpanah, P., "Indicators for Evaluation of Progress in Thermal Stabilization Reactions of Polyacrylonitrile Fibers," *Journal of Applied Polymer Science*, **131**, 11, 2014, pp. 40343-40351.

[29] Janus, R., Natkański, P., Wach, A., Drozdek, M., Piwowarska, Z., Cool, P., and Kuśtrowski, P., "Thermal transformation of polyactrylonitrile deposited on SBA-15 type silica," *Journal of Themral Analysis and Calorimetry*, **110**, 1, 2012, pp. 119-125.

[30] Xue, T.J., McKinney, M.A., and Wilkie, C.A., "The thermal degradation of polyacrylonitrile," *Polymer Degradation and Stability*, **58**, 1997, pp. 193-202.

[31] Piper, D.M., Yersak, T.A., Son, S.B., Kim, S.C., Kang, C.S., Oh, K.H., Ban, C., Dillion, A.C., and Lee, S.H., "Conformal Coatings of Cyclized-PAN for Mechanically Resilient Si nano-Composite Anodes," *Advanced Energy Materials*, **3**, 6, 2013, pp. 697-702.

[32] Grassie, N., and McGuchan, R., "Pyrolysis of polyacrylonitrile and related polymers-II," *European Polymer Journal*, **8**, 7, 1972, pp. 865-878.

[33] Nithya, S., Selvasekarapandian, S., Karthikeyan, S., and Pandi, D.V., "Effect of propylene carbonate of the ionic conductivity of polyacrylonitrile-based solid polymer electrolytes," *Journal of Applied Polymer Science*, **132**, 14, 2015, pp. 1-3.

[34] Piper, D.M., Woo, J.H., Son, S.B., Kim, S.C., Oh, K.H., and Lee, S.H., "Hierarchical Porous Framework of Si-Based Electrodes for Minimal Volumetric Expansion," *Advanced Materials*, **26**, 21, 2014, pp. 3520-3525.

[35] Wang, Z., Huang, B., Huang, H., Chen, L., Xue, R., and Wang, F., "Investigation of the position of Li^+ ions in a polyacrylonitrile-based electrolyte by raman and infrared spectroscopy," *Electrochimica Acta*, **41**, 9, 1996, pp. 1443-1446.

[36] Yang, C.R., Perng, J.T., Wang, Y.Y., and Wan, C.C., "Conductive behaviour of lithium ions in polyacrylonitrile," *Journal of Power Sources*, **62**, 1, 1996, pp. 89-93.

[37] Huang, B., Wang, S., Huang, X., Xue, R., and Chen, L., "Vibrational Spectroscopic Investigation of Polyacrylonitrile-Based Electrolytes with a Dimethylformamide Plasticizer," *Journal of The Electrochemical Society*, **144**, 1, 1997, pp. 44-48.

[38] Huang, B., Wang, Z., Chen, L., Xue, R., and Wang, F., "The mechanism of lithium ion transport in polyacrylonitrile-based polymer electrolytes," *Solid State Ionics*, **91**, 3-4, 1996, pp. 279-284.

[39] Trevey, J., Jang, J.S., Jung, Y.S., Stoldt, C.R., and Lee, S.H., "Glass-ceramic Li_2S-P_2S_5 electrolytes prepared by a single step ball billing process and their application for all-solid-state lithium-ion batteries," *Electrochemistry Communications*, **11**, 9, 2009, pp. 1830-1833.

[40] Takada, K., Aotani, N., Iwamoto, K., and Kondo, S., "Solid state lithium battery with oxysulfide glass," *Solid State Ionics*, **86-88**, 2, 1996, pp. 877-882.

[41] Trevey, J.E., Rason, K.W., Stoldt, C.R., and Lee, S.H., "Improved Performance of All-Solid-State Lithium-Ion Batteries Using Nanosilicon Active Material with Multiwalled-Carbon-Nanotubes as a Conductive Additive," *Electrochemical and Solid-State Letters*, **13**, 11, 2010, pp. A154-A157.

[42] Kitaura, H., Hayashi, A., Ohtomo, T., Hama, S., and Tatsumisago, M., "Fabrication of electrode-electrolyte interfaces in all-solid-state rechargeable lithium batteries by using a supercooled liquid state of the glassy electrolytes," *Journal of Materials Chemistry*, **21**, 118, 2010, pp. 118-124.

[43] Kasavajjula, U., Wang, C., and Appleby, A.J., "Nano- and bulk-silicon-based insertion anodes for lithium-ion secondary cells," *Journal of Power Sources*, **163**, 2007, pp. 1003-1039.

[44] Preiss. H., Szulzewsky, K., and Kölsch, P., "Characterization of pitches by X-ray scattering and differential scanning calorimetry," *Fuel*, **72**, 9, 1993, pp. 1301-1303.

[45] Hubbard, C.R., Swanson, H.E., and Mauer, F.A., "A Silicon Powder Diffraction Standard Reference Material," *Journal of Applied Crystallography*, **8**, 45, 1975, pp. 45-48.

[46] Yang, D.Q., Gillet, J.N., Meunier, M., and Sacher, E., "Room temperature oxidation kinetics of Si nanoparticles in air, determined by x-ray photoelectron spectroscopy," *Journal of Applied Physics*, **97**, 2005, p. 024303.

[47] Morita, M., Ohmi, T., Hasegawa, E., Kawakami, M., and Ohwada, M., "Growth of native oxide on a silicon surface," *Journal of Applied Physics*, **68**, 1990, pp. 1272-1281.

[48] Barnakov, C.N., Khokhlova, G.P., Popova, A.N., Sozinov, S.A., and Ismagilov, Z.R., "XRD Characterization of the Structure of Graphites and Carbon Materials Obtained by the Low-Temperature Graphitization of Coal Tar Pitch," *Eurasian Chemico-Technological Journal*, **17**, 2, 2015, pp. 87-93.

[49] Larcher, D., Mudalige, C., George, A.E., Porter, V., Gharghouri, M., and Dahn, J.R., "Si-containing disordered carbons prepared by pyrolysis of pitch/polysilane blends: effect of oxygen and sulfur," *Solid State Ionics*, **122**, 1-4, 1999, pp. 71-83.

[50] Zheng, T., Xue, J.S., and Dahn, J.R., "Lithium Insertion in Hydrogen-Containing Carbonaceous Materials," *Chemistry of Materials*, **8**, 2, 1996, pp. 389-393.

[51] Zheng, T., Xing, W., and Dahn, J.R., "Carbons prepared from coals for anodes of lithium-ion cells," *Carbon*, **34**, 12, 1996, pp. 1501-1507.

[52] Zheng, T., Liu, Y., Fuller, E.W., Tseng, S., Sacken, U., and Dahn, J.R., "Lithium Insertion in High Capacity Carbonaceous Materials," *Journal of The Electrochemical Society*, **142**, 8, 1995, pp. 2581-2590.

[53] Larcher, D., Mudalige, C., Gharghouri, M., and Dahn, J.R., "Electrochemical insertion of Li and irreversibility in disordered carbons prepared from oxygen and sulfur-containing pitches," *Electrochimica Acta*, **44**, 23, 1999, pp. 4069-4072.

[54] Mochida, I., Ku, C.H., and Korai, Y., "Anodic performance and insertion mechanism of hard carbons prepared from synthetic isotropic pitches," *Carbon*, **39**, 2001, pp. 399-410.

[55] Teki, R., Datta, M.K., Krishnan, R., Parker, T.C., Lu, T.M., Kumta, P.N., and Koratkar, N., "Nanostructured Silicon Anodes for Lithium Ion Rechargeable Batteries," *Small*, **5**, 20, 2009, pp. 2236-2242.

[56] Szczech, J.R., and Jin, S., "Nanostructured silicon for high capacity lithium battery anodes," *Energy & Environmental Science*, **4**, 56, 2011, pp. 56-72.

[57] Whiteley, J.M., Kim, J.W., Piper, D.M., and Lee, S.H., "High-Capacity and Highly Reversible Silicon-Tin Hybrid Anode for Solid-State Lithium-Ion Batteries," *Journal of The Electrochemical Society*, **163**, 2, 2016, pp. A251-A254.

[58] Zhang, W.J., "Lithium insertion/extraction mechanism in alloy anodes for lithium-ion batteries," *Journal of Power Sources*, **196**, 3, 2011, pp. 877-885.

[59] Piper, D.M., Yersak, T.A., and Lee, S.H., "Effect of Compressive Stress on Electrochemical Performance of Silicon Anodes," *Journal of The Electrochemical Society*, **160**, 1, 2013, pp. A77-A81.

[60] Wang, X., Zhang, F.X., Loa, I., Syassen, K., Hanfland, M., and Mathis, Y.L., "Structural properties, infrared reflectivity, and Raman modes of SnO at high pressure," *Physica Status Solidi B*, **241**, 14, 2004, pp. 3168-3178.

[61] Childres, I., Jauregui, L.A., Park, W., Cao, H., and Chen, Y.P., "Raman spectroscopy of graphene and related materials," *New Developments in Photon and Materials Research*, 2013, pp. 1-20.

[62] Chernavskii, P.A., Peskov, N.V., Mugtasimov, A.V., and Lunin, V.V., "Oxidation of metal nanoparticles: Experiment and model," *Russian Journal of Physical Chemistry B*, **1**, 4, 2007, pp. 394-411.

[63] Shin, J.H., Song, J.Y., Kim, Y.H., and Park, H.M., "Low temperature and self-catalytic growth of tetragonal SnO nanobranch," *Materials Letters*, **64**, 9, 2010, pp. 1120-1122.

[64] Jeong, S., McDowell, M.T., and Cui, Y., "Low-Temperature Self-Catalytic Growth of Tin Oxide Nanocones over Large Areas," *ACS Nano*, **5**, 7, 2011, pp. 5800-5807.

[65] Courtney, I.A., and Dahn, J.R., "Electrochemical and In Situ X-Ray Diffraction Studies of the Reaction of Lithium with Tin Oxide Composites," *Journal of The Electrochemical Society*, **144**, 6, 1997, pp. 2045-2052.

[66] Xun, S., Song, X., Battaglia, V., and Liu, G., "Conductive Polymer Binder-Enabled Cycling of Pure Tin Nanoparticle Composite Anode Electrodes for a Lithium-Ion Battery," *Journal of The Electrochemical Society*, **160**, 6, 2013, pp. A849-A855.

LIST OF SYMBOLS, ABBREVIATIONS AND ACRONYMS

ASSB	all-solid-state battery
LIB	lithium ion battery
STN	Si-Ti-Ni
CTP	coal-tar-pitch
PAN	polyacrylonitrile
cPAN	cyclized polyacrylonitrile
PEO	poly(ethylene oxide)
PPO	poly(propylene oxide)
SSE	sulfide solid electrolyte
PEEK	polyetheretherketone
DMF	N,N-Dimethylformamide
SLMP	stabilized lithium metal powder
CC	constant current
FESEM	field emission scanning electron microscopy
EDS	energy dispersive X-ray spectroscopy
FIB	focused ion beam
XRD	X-ray diffraction
SEM	scanning electron microscope
CE	coulombic efficiency
TEM	transmission electron microscope
EELS	electron energy loss spectroscopy

DISTRIBUTION LIST

DTIC/OCP 8725 John J. Kingman Rd, Suite 0944 Ft Belvoir, VA 22060-6218	1 cy
AFRL/RVIL Kirtland AFB, NM 87117-5776	1 cy
Official Record Copy AFRL/RVSV/Jessica Buckner	1 cy

(This page intentionally left blank)